Predicting the flutter speed of a pedestrian suspension bridge through examination of laboratory experimental errors

Fabio Rizzo[1‡*], Luca Caracoglia[2], Sergio Montelpare[3]

[1] CRIACIV (Inter-University Research Center for Building Aerodynamics and Wind Engineering), G. D'Annunzio University of Chieti-Pescara, viale Pindaro 42, Pescara. [1*]fabio.rizzo@unich.it
[2]Department of Civil and Environmental Engineering, Northeastern University, 400 Snell Engineering Center, 360 Huntington Avenue, Boston, MA 02115, USA, lucac@coe.neu.edu
[3] G. D'Annunzio University of Chieti-Pescara, viale Pindaro 42, Pescara, s.montelpare@unich.it

Highlights:

- Standardized protocols for measurement of flutter derivatives are not available.
- Differences in the wind tunnel laboratory methods can induce wind load variability.
- Flutter analysis affected by laboratory setting is studied.
- Critical flutter speeds are estimated for three different bridge deck sections.
- Error analysis of critical flutter speed is conducted using experimental data.

‡ Visiting Scholar, Department of Civil and Environmental Engineering, Northeastern University, 2014

Predicting the flutter speed of a pedestrian suspension bridge through examination of laboratory experimental errors

Fabio Rizzo[1,2‡*], Luca Caracoglia[2], Sergio Montelpare[3]

[1] CRIACIV (Inter-University Research Center for Building Aerodynamics and Wind Engineering), G. D'Annunzio University of Chieti-Pescara, viale Pindaro 42, Pescara, Italy, fabio.rizzo@unich.it (* = corresponding author)
[2] Department of Civil and Environmental Engineering, Northeastern University, 400 Snell Engineering Center, 360 Huntington Avenue, Boston, MA 02115, USA, lucac@coe.neu.edu
[3] G. D'Annunzio University of Chieti-Pescara, viale Pindaro 42, Pescara, Italy, s.montelpare@unich.it

Highlights:

- Standardized protocols for measurement of flutter derivatives are not available.
- Differences in the wind tunnel laboratory methods can induce wind load variability.
- Flutter analysis, affected by laboratory setting, is studied.
- Critical flutter speed is estimated for three different bridge deck configurations.
- Error analysis of critical flutter speed is conducted using experimental data.

Abstract

The paper investigates experimental error propagation and its effects on critical flutter speeds of pedestrian suspension bridges using three different experimental data sets: pressure coefficients, aerodynamic static forces and flutter derivatives. The three data sets are obtained from section model measurements in three distinct laboratories. Data sets are used to study three different geometries of pedestrian suspension bridges. Critical flutter speed is estimated using finite- element nonlinear analysis, numerical 2-DOF generalized deck model and 3-DOF full-bridge models. Flutter probability, contaminated by various experimental error sources, is examined. Experimental data sets are synthetically expanded to obtain two population sets of deck wind loads with 30 and $5 \cdot 10^5$ realizations, respectively. The first set is obtained using Monte-Carlo simulation approach, whereas the second one is determined using Polynomial chaos expansion theory and a basis of Hermite polynomials. The numerically-determined probability density functions are compared against empirical probability histograms (*pdfs*) by Kolmogorov-Smirnov tests.

Keywords: pedestrian suspension bridge; flutter; aerodynamic and aeroelastic tests; pressure coefficients; experimental error analysis.

1. Introduction

Conurbations are more and more affected by traffic pollution, leading to a policy trend that promotes public transportation and pedestrian and bicycle pathways. Many governmental master plans contemplate new "green roads" around downtowns, across rivers or highways. The goal is to

‡ J-1 Visiting Scholar, Department of Civil and Environmental Engineering, Northeastern University, 2014

create a comfortable alternative way to get around town. Pedestrian bridges play a fundamental role as part of this trend because they are an efficient way to connect different neighborhoods of a large city.

One of the critical aspects of pedestrian bridges is their impact on the natural environment due to the presence of either pillars, substructures or support structures. River crossings are especially critical because, in order to reduce the bridge span, pillars are often located in the waterway. This aspect often causes controversies between designers and ecologists regarding preservation of the natural ecosystem. Examples of pedestrian bridges with intermediate supports are: the London Millennium Footbridge (2000) that has a total length equal to 325 m and a central span length equal to 144 m, the Puente de La Mujer (2001), Buenos Aires, Argentina with a total length equal to 170 m but with its longest span equal to 102.5 m and the Goodwill Bridge, crossing the Brisbane River in Brisbane, Queensland, Australia, which has a total length of 450 m with its longest span equal to 102 m. Another recent example is the Sea Bridge on the Pescara River in Pescara, Italy [1] . This structure is the longest pedestrian-and-bicycle bridge in Italy and one of the longest in Europe. Its total length is 466 m and the length of the longest central span is 172 m.

Pedestrian bridges with increasing spans require larger sub-structures; this need leads to higher costs. The deck section height and width are influenced by span length. Suspension bridges could be used for pedestrian bridges to obtain long spans and minimize the risk of environmental interferences. This solution, using a typical scheme such as the one illustrated in Fig.1a, permits structural construction with a single large span. In this standard configuration, the pillars are used in conjunction with parabolic cables for the main span and "back" stay-cables for the lateral spans [2] , [3] . However, this geometrical configuration may be invasive near rivers since the use of multiple spans could negatively affect integration of the bridge with the urban context. For this reason, the solution illustrated in Fig.1b may be more successful for pedestrian bridges. This solution has inclined pillars to counteract large internal tension forces originating from main suspension cables through tower anchorages.

The lightness and slenderness of pedestrian suspension bridge decks are the cause of two main structural problems: resonance in footbridges due to large lateral vibration, induced by walking pedestrians ([4] [5] [6] [7] [8] [9] [10] [11] [12] [13] [14] [15]), and flutter instability induced by wind loads. Both aspects are extensively investigated in the literature. The latter aspect, in particular, has been has been comprehensively studied in wind engineering for large span vehicular suspended bridges; several studies have proposed models and methods for the reliability analysis of vehicular bridges sensitive to flutter instability.

A general discussion on bridge flutter is presented, for example, in Zasso et al. [16] who examine the state of the art in the field of bridge aerodynamics, describing a number of procedures for evaluating not only flutter stability but also turbulence-induced buffeting response, and in Pourzeynail and Datta [17] . Two important examples of systematic approach for flutter reliability analysis are: the model proposed by Ge et al. [18] , which is formulated as a limit state threshold-crossing problem and a probability calculation approach to determine the probability of bridge failure due to flutter; and by Cheng et al. [19] , who propose a reliability analysis method by combining the advantages of the response surface method, finite element method (FEM), first-order reliability method and the importance sampling method..

Bridge flutter instability is primarily investigated by studying the aerodynamics and aeroelastic behavior of the deck section [20] [21] . In the technical literature this aspect is examined using appropriately scaled deck section models, tested in wind tunnel to estimate aerodynamic forces (Lift, Drag and Moment) both directly (force measurements) and indirectly (pressure measurements), and to evaluate the flutter (or Scanlan) derivatives of the deck section [22] , [23] . Static and dynamic experiments are often conducted to study bridge instability phenomena. For example, Argentini et al. [24] describe experimental and numerical analysis of the dynamic response of a cable-stayed bridge with a focus on vortex induced vibrations and buffeting effects; Diana et al. [25] [26] present a comparison between wind tunnel tests conducted on a full-bridge aeroelastic model of the proposed suspension bridge over the Strait of Messina (Italy). Similarly, Argentini et al. [27] compare wind tunnel tests carried out on a full aeroelastic model with numerical results for the Izmit Bay Bridge (Turkey). Several other literature studies have considered issues related to flutter derivatives, mostly focused on the dependence between flutter derivatives and deck section geometry. One representative example is the study by Scanlan et al. [28] that analytically derive the interrelations and approximate correspondences among flutter derivatives of a bridge deck, derived from theoretical low-speed airfoil aeroelasticity. Another significant example is the study by Matsumoto et al. [29] , which focuses on the influence of each flutter derivative on flutter instability, obtained by pressure measurements on the side surface of 2-D rectangular cylinders with B/D side ratios (B is the chord length, D the deck height) between 5 and 20 and examining 1DOF coupled heaving/torsional forced vibration.

Frequently, flutter instability studies are specifically applied to case studies. For example, Lau and Wong [30] studied the aerodynamic stability of the Tsing Ma Bridge; Zdravkovich and Carelas [31] investigated the aerodynamics of a covered pedestrian bridge with a trapezoidal section. Parametric studies are particularly interesting because they examine the same phenomenon using different case studies or structures. This methodology was used, for example, by Zhang and Sun

[32] who proposed parametric analyses of the aerodynamic stability of the Runyang Bridge over the Yangtze River, including the structural system. This paper adopts a similar study methodology and examines the design parameters that influence wind-induced aerodynamic stability of a pedestrian bridge by identifying the "most favorable" structural system.

Despite all the advances in the theory of flutter and buffeting of long span bridges [33] several unresolved issues are still present and often overlooked in the case of pedestrian suspension bridges. The present paper, following a parametric approach, investigates flutter instability of three closed-box deck sections [34] applied to the design of pedestrian suspension bridges. This paper focuses on the flutter instability and studies the influence of experimental measurement error on critical flutter speed. In wind engineering the issue of uncertainties in the experimental details and their effects on structural reliability have been extensively investigated (e.g. [21] [35]). This aspect is particularly important when the goal of the experiments is to predict the critical flutter speed for suspension bridges (e.g. [36] , [37]).

The present study considers three different types of wind tunnel experiments, conducted in three different laboratories: static pressure measurements and flutter derivative measurements on various deck section models, [38] [39] [25] [40] [32] . Experimental results are also compared against literature data with similar bridge deck shape and geometry.

Wind tunnel experiments of three deck section models were carried out, estimating drag, lift and moment both directly (force measurements) and indirectly (pressure measurements). Aeroelastic wind tunnel tests were conducted to estimate the flutter derivatives of one of the three models [23] .

Critical flutter speed was subsequently predicted, using the three experimental data sets, by two methods: three-dimensional finite element analyses and 2-DOF numerical analyses [40] . Quasi-static simplified analysis (e.g. [28]) was employed to derive the flutter derivatives from the experimental sectional aerodynamic loads (drag, lift and moment). Verification of the quasi-static analysis was investigated using results from one of the aeroelastic tests on a 2-DOF model [41] , [28] .

The dependence of critical flutter speed on the geometries of the deck section was investigated using the experimental data sets and both analysis methods. Experimental errors induced by laboratory experimental conditions were integrated to enable flutter reliability analysis. For reliability analysis purposes, a large sample of random aerodynamic input data was needed. Two sample sizes were used: 30 realizations and $5{\cdot}10^5$ realizations, respectively. Expansion with 30 realizations from the original experimental data sets was obtained by Monte-Carlo simulation [42] , [43] , whereas expansion with $5{\cdot}10^5$ realizations was carried out by Polynomial chaos (PC) expansion (e.g. [44] , [45]). Results were critically examined by studying the probability density function (*pdf*) of the critical flutter speed [46] .

2. Wind tunnel experiments

Static and dynamic tests were carried out to estimate the deck loads of a benchmark pedestrian bridge with closed-box bridge deck (structural properties are described later in a subsequent section). Static tests conducted on a rigid model of the deck section included two sets of measurements. The first one evaluated the aerodynamic forces (drag, lift and moment per unit length) (S-tests in the following) [11] , [12] . The second set measured the pressure coefficients along the surface of the closed-box section (P-tests in the following). Dynamic tests (D-tests in the following) were conducted to estimate the flutter derivatives. Quasi-static flutter derivatives, approximately estimated from the static forces found by the S-test, were also considered in the subsequent comparisons (e.g. [28] , [34]). It is important to note that, in this study, the deck guardrail was neglected because it was assumed that it was made of cables and, therefore, would not affect the aerodynamics and the aeroelastic response [47] .

2.1 Cross-sectional geometry and properties of the examined deck models

Three deck section configurations were chosen to study the influence of aerodynamic effects on the flutter speed of a pedestrian bridge. They are illustrated in Fig. 2. The main dimensions of the bridge structure in Fig. 2 are selected as follows: H_1 = 45 m, H_2 = 15 m, L_1 = 494 m, L_2 = 584 m, L_3 = 45 m and f =3 m. Detailed geometric properties of the deck sections are listed in Table 1. The three deck section configurations are: MOD1 (Fig. 2a), MOD2 (Fig. 2b) and MOD3 (Fig. 2c). All the sections have the same height (h_1+h_2), total width (b_1+b_2+b_1) but a variable d_2 dimension.. Values of d_2 are (in relative terms) small (MOD3), medium (MOD2) and large (MOD1). The reason for this choice is to examine a wide range of configurations [34] .

2.2 Aerodynamic wind tunnel tests

S-tests and P-tests were carried out using rigid wind tunnel models with the same dimensions. The tests were designed to minimize any potential discrepancies induced by geometric scaling differences. The models were made of wood. Appropriate flexural rigidity of the models was carefully assessed before the tests. The geometry of the experimental models is described in Table 1 for each section (Fig. 2). Dimensions in the figures and for both test cases are in millimeters (mm). Section model dimensions are: 1000 (ℓ, spanwise length) by 40 (H, height) by 292 (B, chord or width), with a geometrical aspect ratio ℓ/B equal to 3.43. In both experiments, mean flow speed was approximately the same (about 14.5 m/s) and the turbulence intensity was very low.

2.2.1 *Aerodynamic forces (S-tests).*

S-tests were carried out in the wind tunnel of the Marche Polytechnic University (Ancona, Italy). The wind tunnel is a closed-circuit facility as shown in Fig. 3. The cross-sectional dimensions of the main test chamber are about 1.8 m by 1.8 m. The main test section has three main test subsections: the first one is used for aerodynamic tests requiring uniform velocity distribution and low turbulence level. The second one is used to test aerodynamic interference between slender bodies. The last one is the environmental section where atmospheric boundary layer flows can be reproduced for general studies on buildings and structures. The wind tunnel is equipped with a motor/fan having a constant rotational speed (975 rpm) and 16 blades with adjustable pitch. The mean wind speeds range between 6 m/s and 40 m/s. Preliminary flow measurements, using a Constant Temperature Hot Wire Anemometer, showed a deviation less than 2.5% from the reference value of the mean flow speed and longitudinal turbulence intensity less than 0.3% across more than 90% of the test cross section. A compact heat exchanger was used to control temperature fluctuations within the range of ±1 [°C]. Fig. 3c presents a picture of a typical setup of the chamber with the experimental model. The same was done for the P-tests with a sampling frequency equal to 500 Hz and an acquisition time of 60 s.

The purpose of these tests was to measure the Drag (D), Lift (L) and Torsional Moment (M) of the deck per unit span for the three geometries, illustrated in Fig.2. The average values of drag, lift and torsional moment coefficients per unit span, respectively C_D, C_L and C_M, were evaluated according to Eq. 1 below. The corresponding graphs are illustrated in Figs. 4a, b and c as a function of the angle of attack. In Eq. 1 U is equal to 14.5 m/s, ρ is equal to 1.18 kg/m^3 and, referring to Table 1, B is the reference width equal to $2d_1+b_1$= 298 mm. The model was placed vertically, as visible from Fig. 3b, and the reference system for the calculation of the aerodynamic forces is given in Fig. 3d. Twenty-one values of attack angle (α) were considered in the interval between -10° and +10°. Positive angles are "nose up" in relation to the approaching flow.

$$C_D = \frac{D}{\frac{1}{2}\rho U^2 B}\ , \qquad C_L = \frac{L}{\frac{1}{2}\rho U^2 B}, \qquad C_M = \frac{M}{\frac{1}{2}\rho U^2 B^2} \tag{1}$$

Preliminary load balance measurements were carried out at different flow speeds (i.e. 6.3, 8.3 and 14.8 [m/s]) and the results collapsed on the same curves once the experimental values were rearranged in the form of dimensionless parameters (i.e. C_D, C_L and C_M). This behaviour confirmed the absence of Reynolds number dependence for the tested range of flow speeds and, consequently, subsequent measurements (i.e. the ones reported in this paper) were conducted at the higher velocity in order to obtain an output signal with larger magnitude and increase accuracy. Examination of experimental results and a comparison of the aerodynamic coefficients C_D, C_L and C_M in Figs. 4 a, b and c suggests that MOD2 and MOD3 have a similar aerodynamic behavior, quite distinct from the one exhibited by MOD1. On average, for positive angles the C_D of MOD1 is smaller than the one of MOD2 and MOD3 in the interval -6°≤α≤10°, whereas in the interval -10°≤α≤-6° MOD2 has the smallest C_D values. With regard to C_L, MOD1 has the smallest values whereas MOD3 has the biggest ones. All models exhibit a similar trend and values of C_M. For negative angles MOD3 has C_M values slightly larger than those of the other two models, whereas for positive angles this goes for MOD2.

To summarize, MOD1 globally has the smallest value of aerodynamic coefficient (i.e. except for few negative angles of C_D). The aerodynamic coefficients of MOD3 are larger than the ones of other models (i.e. except for few negative angles of C_D).

For negative attack angles, the absolute values of C_L and C_M of MOD1 are larger than those of the other two models. This observation suggests that that both L and M tend to increase (absolute value) when the dimension b_2 decreases (Table1 and Fig. 2). The trend is opposite for positive angles α: a decrement of b_2 induces a decrement of L and M. In Fig. 4 the aerodynamic coefficients, evaluated by integrating the pressure coefficients (as described in the subsequent section), are also presented. The two sets of measurements are overlapping. The trend is confirmed and the values are very similar.

Figure 4 also illustrates the comparison between data sets MOD1, MOD2, MOD3 and the Great Belt deck static aerodynamic coefficients reproduced from Reinhold et al. [51] and Scotta et al. [50] α=0° (Figs. 4c and d). The Great Belt Bridge was selected as the benchmark deck structure for comparison of the test results; this is also a single closed-box girder, with geometry approximately similar to the one of the models experimentally examined in this study. The overlap among the various data sets shows a satisfactory agreement between the Great Belt data and MOD2 values for C_D (Fig.4a), MOD3 values for C_L (Fig.4b), and MOD3 values in the range of -2≤α≤2 for C_M. Larger differences are noted in other cases.

2.2.2 Pressure coefficients (P-tests)

The *P-tests* were carried out in the CRIACIV (Inter-University Research Centre for Wind Engineering and Building Aerodynamics) boundary layer wind tunnel in Prato (Italy), Fig. 5a and 5b. This is an open-circuit wind tunnel with a reference test section, which is 2.42 m wide and 1.60 m high. The total length of the wind tunnel is about 22 m. Wind speed is regulated both by adjusting the pitch of the ten-fan blades and by controlling its angular speed of the motor [49] . The maximum wind speed is about 30 m/s. The models were horizontally placed in the wind tunnel; they were rigidly connected to a support system, composed of rigid arms, as illustrated in Fig. 5e. The sampling frequency during the tests was about 500 Hz and the acquisition time was 60 s. Tests were carried out at three mean flow speeds U (3.5, 8.5 and 14.5 m/s) also to investigate the Reynolds number dependence. The turbulence intensity was on average less than 1% (i.e. slightly larger than the one used for *S*-tests). The standard deviation of speed and turbulence was between about 0.1 m/s and 0.2%, respectively.

Static pressures were evaluated and normalized in accordance with the reference dynamic pressure, as in Eq. 2. The dimensionless pressure coefficient (C_p) was estimated from the difference between the static pressure measured at each pressure tap (p_i) and the reference flow static pressure p_0 [24] .

$$C_p = \frac{p_i - p_0}{\frac{1}{2}\rho U^2} \tag{2}$$

The experiments had confirmed that the dependence can be neglected in this case.

Figs. 5c and 5d illustrate the location of the pressure scanner, inside the model. Figure 5c shows the system of pneumatic connections; Fig. 5d presents a three-dimensional view of the pressure tap positions. Three strips of 40 pressure taps were simultaneously used for each model. The external pressure coefficient distributions for all the three models were evaluated at fifteen angles of attack (α): 0°; ±1°; ±2°; ±3°; ±4°; ±6°; ±8°; ±10°. The photograph in Fig. 5e is an example of a typical pressure test; Fig. 5f illustrates the reference coordinate system used in the wind tunnel. The mean pressure coefficient values ($C_{p,m}$) are plotted and illustrated in Figs. 6-8 for each angle of attack. The plotted values refer to the cross section located at the center of the model. A negative pressure coefficient represents suction while a positive value represents overpressure. Experimental results were approximately the same independently of mean flow speed.

The wind tunnel blockage was estimated considering the model, end plates, anchorages and support structures of the test rig and; it is variable between 2% (α=0°) and 15% (α=±10°). For this reason, a correction was applied to each value of mean wind speed used in Eq. (2) [4] . Despite the corrections, the $C_{p,m}$ positive values are close to the stagnation pressure 1 but, on occasion, possibly exceed 1.0, as for example for α=±10°. A small discrepancy is reasonable in these extreme cases as it may be influenced by the fidelity of the pressure measurement system and the accuracy of the test setup.

Figures from 6 to 8 illustrate the pressure coefficients of all bridge section decks (i.e. MOD1, MOD2 and MOD3) and for all angles (i.e. -10°≤α≤10°). Experimental results show many differences between lower and upper surfaces of the deck and between negative and positive angles. Local values of mean pressure coefficients are compared in the following.

On the lower surface the largest negative pressure value (negative mean pressure coefficients), for negative angles of attack, is -2.54 for MOD3, -2.05 for MOD2 and -1.56 for MOD1. For positive angles of attack, it is -1.19 for MOD3, -1.07 for MOD2 and -1.05 for MOD1. MOD1 has the smallest suction values for both negative and positive angles.

On the upper surface the largest negative pressures (suctions) is, for negative angles, -0.99 for MOD2, -0.96 for MOD3 and -0.74 for MOD1. For positive angles the largest negative pressures are -2.50 for MOD3, -2.43 for MOD2 and -2.09 for MOD1. Overall, MOD1 has the smallest suction values for both negative and positive angles.

In summary, analyzing both upper and lower surfaces of the bridge deck section, MOD1 has the smallest local pressure coefficients for negative and positive angles, whereas MOD3 has the biggest local pressure coefficients for positive angles α except for negative angles on upper surface for which MOD2 has a slightly bigger value than MOD3.

Figs. 9a and 9b present a comparison between mean pressure coefficients for angles of attack α={-10°, 0°, 10°} by examining both upper and lower surfaces of the deck, respectively. The graphs show on the horizontal axis the normalized abscissa x/B, measured from left to right across the sections portrayed in Fig.2; the mean pressure coefficients are displayed on the vertical axis.

On the upper surface (Fig.9a, 9c and 9e) all models exhibit similar trend and values, even though MOD2 has slightly bigger positive value for α=-10° in the range $0 \leq x/B \leq 0.1$ (Fig. 9a). Overall, the largest differences between the geometries on the upper deck surface, for α=-10° and α=10° (Fig. 9e), are located inside the flow recirculation zone ($0 \leq x/B \leq 0.1$), whereas for α=0° the values are very close with a slight difference in the range $0.8 \leq x/B \leq 1.0$.

On the lower surface of the deck (Figs. 9b, 9d and 9e) the trend of the mean pressure coefficients is different among the various cases (MOD1, MOD2 and MOD3). In particular, differences are evident for α=-10° (Fig.9a) in the $0 \leq x/B \leq 0.6$ range; it is observed that MOD3 has the largest negative pressure peak but the overall magnitude of the negative pressures is smaller than the one of other cases for a large region of the deck. All the models have very similar values in the range $0.6 \leq x/B \leq 0.9$. For α=0° (Fig.9d), the pressure coefficients of MOD2 and MOD3 are very similar and quite different from MOD1. Finally, for α=10°, values are close for all geometries in the ranges $0 \leq x/B \leq 0.3$ and $0.7 \leq x/B \leq 0.1$. Based on the experimental results and observing the mean pressure coefficient trends for the three representative angles considered α={-10°, 0°, 10°}, there is partial correspondence between the model that has the largest or smallest local pressure coefficients and the model with consistently smaller or larger pressure coefficients. This observation is in line with the previously described trend, estimated with the S-tests. However, the pressure coefficient results, obtained with the S-tests on the lower deck surfaces, suggest that the aerodynamic behavior of MOD1 is fairly different from the other models.

Figure 9c and d (i.e. α =0°) also show the values of mean pressure coefficients for the Great Belt Bridge deck, reproduced from [50] [51] and used for comparison purpose as in the previous sub-section. On the upper surface of the deck, the overlap shows a satisfactory agreement with MOD3. In contrast, on the lower surface of the deck in the range $0 \le x/B \le 0.2$ the Great Belt Bridge pressure coefficients are close to MOD1; in the range $0.2 \le x/B \le 0.4$ values are intermediate between MOD1 and MOD3; finally, in the range $0.4 \le x/B \le 1.0$ the $C_{p,m}$ distribution is very close to MOD3.

2.3 Aeroelastic wind tunnel tests

The main aeroelastic forces induced by the motion of the deck were based on the formulation by Scanlan and Tomko [23] . These are the lift force L_h and the overturning moment M_α, measured as quantities per unit deck length on a section model of span length ℓ. The expressions are found in Eqs. (3) and (4) below (noting that the sign of the lift force L_h is usually opposite compared to L previously defined). The quantities H_i^* and A_i^* (with i=1,…,4) are the Scanlan (or flutter) derivatives [23] that depend on reduced frequency $K=\omega B/U$ or, equivalently, reduced wind speed $U_r=U/(nB)=2\pi/K$, with $\omega=2\pi n$ being the angular frequency of the deck vibration (rad/s) and n the frequency in Hz.

$$L_h = \frac{1}{2}\rho U^2 B\left[KH_1^*(K)\frac{\dot{h}}{U} + KH_2^*(K)\frac{B\dot{\alpha}}{U} + K^2H_3^*(K)\alpha + K^2H_4^*(K)\frac{h}{B}\right], \tag{3}$$

$$M_\alpha = \frac{1}{2}\rho U^2 B^2\left[KA_1^*(K)\frac{\dot{h}}{U} + KA_2^*(K)\frac{B\dot{\alpha}}{U} + K^2A_3^*(K)\alpha + K^2A_4^*(K)\frac{h}{B}\right]. \tag{4}$$

In Eqs. (3) and (4), valid for simple harmonic motion of the deck [23] , ρ is the air density, U the mean wind speed perpendicular to the bridge model's axis, B is the deck width; the over-dot symbol denotes derivation with respect to time t. The quantities h and α are the instantaneous heaving motion and torsional angle of the deck section; lateral sway motion component and drag force are not considered in this study as their contribution to flutter is usually less important apart from special bridge cases [52] .

Aeroelastic tests (D-tests in the following) were used to estimate the flutter derivatives of one of the three geometries and to compare the estimated critical flutter speed with the results obtained using S- and P-test data. The tests were carried out using section model MOD2.

A 2-DOF aeroelastic force balance was employed to determine L_h and M_α [4] . The balance reproduces the vertical (h) and torsional (α) vibration of a representative section model of a bridge deck in the wind tunnel. The free-vibration experimental method was employed to estimate the derivatives (e.g. [22] and [23]).

Tests were conducted in the small-scale wind tunnel of Northeastern University (Boston, Massachusetts, USA) [53] . The tunnel has a test section of 0.56 m by 0.56 m. It is capable of producing wind speeds up to about 20 m/s with low turbulence. The main model dimensions, in mm, are equal to 530 (ℓ , spanwise length) by 20 (H, height) by 148 (B, chord), with a geometrical aspect ratio ℓ/B equal to 3.57. The blockage effect was less than 1% and was therefore negligible. Preliminary experiments were carried out to calibrate the apparatus. The wind tunnel chamber is presented in Fig. 10a; the test rig is illustrated in Fig. 10b and c. The photograph in Fig. 10d depicts a typical experimental setup; Fig. 10e gives the reference coordinate system used to determine the flutter derivatives.

The mean flow speed in the wind tunnel was varied between 2 m/s and 9 m/s, i.e. U={1.90, 2.64, 3.38, 4.25, 5.30, 6.26, 7.43, 8.40} m/s. Both 1-DOF (h vertical motion only) and 2-DOF (both h vertical and torsional α motions) experiments were performed. The model mass per unit length (m) was equal to 2.743 kg m^{-1}; the polar moment of inertia per unit length (I) was equal to 0.010 kg m^2 m^{-1}. The vertical- and torsional-DOF vibration frequencies ($\omega_h/2\pi$ and $\omega_\alpha/2\pi$) were respectively 3.89 Hz and 6.74 Hz. The frequency ratio was designated as $\varepsilon=\omega_\alpha/\omega_h$. Finally, the reduced wind speed (U_r) was used to plot the test results after extraction of the flutter derivatives H_i^* and A_i^*.

Prior to identification of the flutter derivatives, the Power Spectral Density (PSD) was used to identify the main frequency components in each experiment. Examples of PSD graphs are reported in Fig. 11a and Fig. 11b, respectively for 1-DOF and 2-DOF tests. The ratio between torsional and vertical frequency is $\varepsilon\approx1.7$. Structural damping ratios of the 2-DOF moving setup (ζ_h and ζ_α) were evaluated in absence of wind flow. These quantities were later used for identification of H_i^* and A_i^*. Mean values of ζ_h and ζ_α were, respectively, 0.36% and 0.85%. Flutter derivatives (mean curves) are presented in Figs. 11c and 11d. The quantities H_i^* and A_i^* with i=1,…,4 are illustrated. The flutter derivatives were determined using the Iterative Least Squares method [55] at each flow speed, or reduced wind speed. Thirty repeated acquisitions were considered to examine the experimental uncertainty [56] . Data acquisitions were subsequently averaged (sample mean) at each reduced wind speed to obtain the data points summarized in Fig. 11c and 11d. Extremely small positive values were experimentally found for A_2^* at low reduced wind speed in the range between 3 to 5. Figures 11 e and f illustrate the comparison between MOD2 and the Great Belt Bridge flutter derivatives, reproduced from the literature [13] [17] [51] [57] . The figures show a satisfactory agreement, especially for A_2^* and H_3^*.

Test results were subsequently used to evaluate the critical flutter speed of a full-scale pedestrian bridge in accordance with a 2-DOF numerical model (Section 4.2). The characteristics of the full-scale structure were based on the results of a preliminary nonlinear structural analysis (Section 3).

3. Structural design of the pedestrian bridge deck and suspension cables

Three designs of suspension pedestrian bridges were considered, as described in Section 1 and Table 1. Each structural model was constructed by considering one of the deck cross-sectional shapes at a time; the geometry of the deck cross-section leads to a variation in the physical and structural properties of the structure. The selected design simulates a deck structure built by hollow-structural steel pipes (Fig. 12). A wood deck surface and a thin -layer metal deck were used to simulate the superstructure. Static and dynamic analyses were carried out to design the three pedestrian bridge structures. Various load combinations were considered in the design. Dead loads were estimated as equal to 0.3kN/m^2. The live load was assumed to be equal to 5 kN/m^2 and snow load equal to 2 kN/m^2. Static wind pressure was used in the preliminary design of the structure. It was evaluated using a 30 m/s reference wind speed and the pressure coefficients illustrated in Figs. 6-8.

Deck flexural I_x and torsional J_g equivalent inertias are listed in Table 2. The typical pipe size (diameter, ϕ and wall thickness, s) and moments of inertia are listed in Table 2 for each model. The yield stress of the steel is assumed equal to 325 MPa. Figs. 12a to c present a schematic view of the deck section structural model for each geometry.

The center-to-center distance between the two main suspension cables is about 10 m for all geometries. For the hangers, initial strain $\varepsilon_{h,0}$ and section area A_h are listed in Table 2. Values were preliminarily fixed using a simplified 2D model under gravitational static loads. The main cable areas A_c and strain $\varepsilon_{c,0}$ were calculated and updated using the catenary method; the values are summarized in Table 2. The Young's modulus of the cables is equal to $1.65 \cdot 10^8$ kN/m^2. Cable areas and strains were calibrated to obtain vertical displacements smaller than $1/1000L_1$ (Fig.2, Section 2.1) under live loads. Finally, F is the structural dead load per unit span length. Fig. 12d illustrates the local structural model of the tower and Fig. 12e shows the finite element model of the full bridge. The comparison of the values in Table 2 suggests that the structural mass of MOD1 is the lowest, because of a smaller girder dimension and smaller design wind loads, evaluated from the pressure coefficients given in Figs. 6 and 7.

Tower height (Fig.12d) is approximately 60 m and tower weight is approximately 5000 kN (approximately 85 kN/m). In this preliminary design phase, one type of steel pipe section was exclusively used with a diameter of 450 mm and a wall thickness equal to 8 mm. Fig. 12d presents the schematics of the finite element model of the tower. Four vertical stabilizing cables of 250 mm diameter and pre-tensioned at a 0.28% strain can be noted. The tower design accounts for the horizontal component of the internal axial force of the main cables. All the calculations are carried out according to Eurocode 1 [58] .

Geometric non-linear analyses were carried out using a research and design software program (TENSO), which enables non-linear dynamic analysis of wind-structure interaction at flutter. The bridge deck model was simplified by a beam model located in the deck section's center of gravity and two massless rigid links to simulate the connection of the deck to the hangers and cables. Modal analysis was carried out to estimate natural frequencies. The frequencies of the first symmetric and asymmetric vertical and torsional modes are listed in Table 3 for each of the three bridge configurations. The frequency ratio between the symmetrical modes is about 1.42 to 1.64. Fig. 13 illustrates, for MOD1, one example of mode shapes for the fundamental bridge modes listed in Table 3. The mode shapes of other configurations are similar and are not reported for the sake of conciseness. Figure 14 presents, for each structural configuration, deck vertical displacements and rotations of the fundamental modes listed in Table 3. In each panel, vertical displacements (δ) and rotations of the deck about the longitudinal bridge axis (α_x) are plotted in normalized format (i.e. upward deck displacements are positive and counterclockwise rotations are positive); the mode shape functions are normalized so that the norm of the discrete eigenvector is equal to one. Structural damping coefficient for this kind of structure is usually low. In the numerical investigations, damping ratios between 0.1% and 0.5% [2] were used to study how damping influences the critical flutter speed of each structural configuration. The main results of the numerical simulations are summarized in the next section.

4. Deterministic Flutter Analysis

The critical flutter speed was estimated using two different approaches: first, nonlinear dynamic analysis by three-dimensional finite element models and quasi-static approximation of the unsteady wind loads (i.e. lift, drag and moment derived from the wind tunnel tests) were employed; second; a two-mode (2-DOF) generalized numerical model of the deck motion in the frequency domain and flutter derivatives were considered to more correctly examine bridge aeroelasticity.

4.1 FEM analysis

Nonlinear dynamic flutter analysis (in the following NM), [59] , [60] , was carried out using the aerodynamic coefficients reported in Fig. 4 in accordance with the reference force system reported in Fig. 3d, [61] . The analyses were performed using the TENSO nonlinear geometrical analysis program, which can execute dynamic step-by-step integration of the nonlinear three-dimensional structure with geometric nonlinearities.

The TENSO software includes modules for simulating cable and beam finite element models and for the study of wind-structure interaction phenomena with generation of wind speed time histories and simulation of various aeroelastic loads. The main cables are discretized as rectilinear cable segments. The global stiffness matrix is updated at each load step by assembly of the stiffness sub-matrices of the elements, updated to account for the strain found at the previous time step. In this way the software considers the geometric nonlinearity of the structure.

The TENSO software first solves for the static equilibrium of the structure under dead, gravity and construction loads (prior to the application of the wind loads) by nonlinear static analysis; two methods are simultaneously used: step-by-step incremental method and a "subsequent interaction" method with variable stiffness matrix (secant method). The secant method is a finite-difference approximation of the Newton-Raphson's modified method for systems of nonlinear algebraic equations [20] [21] [20] . The solution under gravity loads is subsequently used as the initial step of the dynamic wind load analysis. The Newmark-Beta method with Rayleigh damping is used for numerical integration of the dynamic equations. Wind loads on the bridge deck are time dependent; they are simulated by applying the aerodynamic coefficients (C_D, C_L and C_M) as a function of the time-dependent angle of attack and by setting the appropriate values of dynamic wind pressure at a given mean wind speed U (at deck level). The program evaluates displacements and rotations of the bridge deck at progressively increasing values of U, and records the velocity at incipient flutter when the reference deck vibration amplitude exceeds ±5°. Fig. 15 illustrates three examples of NM time histories exhibiting flutter instability in terms of vertical deck displacement (δ) and rotation (α), for the middle-span section (i.e. upward displacements are positive and counterclockwise rotation are positive).

4.2 Equivalent 2-DOF Scanlan's numerical model

Equations (3) and (4), presented in a previous section, must be modified to enable estimation of critical flutter speed in the frequency domain. Incipient flutter is determined from a condition coincident with the simple harmonic motion of the deck accounting for coupled vertical and torsional motion (DOFs). This condition is determined by the vanishing of the total damping (i.e.

including structural damping and the contribution of aeroelastic load interaction) of a 2-DOF generalized model, which simulates the two fundamental, vertical and torsional modes of the deck. Even though more sophisticated approaches are currently employed for flutter examination on long-span bridges (e.g. multi-mode approach [52]), the equivalent 2-DOF model, described in this section, was considered appropriate for the present investigation, mainly focusing on experimental error and modeling uncertainties. Additional studies will possibly be considered in the future.

The procedure for finding flutter is recursive. The method (designated as SM in the following), described in Simiu and Scanlan [40] , was used. In the flutter calculations, the derivatives H_i^* and A_i^*, with $i = 1,2,3$ and as a function of $K=2\pi nB/U$, were employed. Flutter calculations were conducted by neglecting the contribution of H_4^* and A_4^*. Solution to the flutter problem using the 2-DOF generalized model can be obtained by transforming the differential system into a system of two complex-valued algebraic equations. After imposing the flutter condition, the roots of these two algebraic equations (available in Simiu and Scanlan [40] and not reported herein for the sake of brevity) can be found numerically. A recursive method was used, setting the value of the reduced frequency K first and finding the root of each equation in terms of the unknown variable $X = {}^{\omega_c}/\omega_h$; the quantity ω_c is the critical angular flutter frequency and ω_h is the angular frequency of the vertical DOF or deck mode (or generalized model). The iterative procedure was repeated until the same real root X was found in both equations.

4.3 Critical flutter speed

The flutter critical speed (in the following designated as U_c) was evaluated by both methods (i.e. NM and SM) described in Section 4.1 and 4.2, using all experimental data described in section 2 (i.e. S-tests, P-tests and D-tests). Results are summarized in Table 4. Critical flutter speed determined by NM were evaluated using aerodynamic forces directly acquired by S-tests and indirectly calculated by P-tests. In contrast, critical velocities were determined by SM using flutter derivatives either experimentally measured (MOD2 only) or estimated using quasi-static equivalent method [28] [41] , after processing the P-test and S-test data. Numerical calculations were repeated by varying the modal damping ratio (ξ) between 0.1% and 0.5% (Section 4.1). It is important to note the damping is constant for SM analyses, whereas it is approximately constant in the NM analyses (calibrated using Rayleigh damping); this small difference partially explains the differences in the results.

Examination of Table 4 confirms that the critical flutter value increases when damping increases. Structural damping influences the results with all experimental data (P, S and D-tests) and using both flutter calculation procedures (NM and SM). This remark suggests that damping must be adequately estimated to determine the flutter instability threshold. Since the objectives of this study are the investigation of variability in the measurement of aerodynamic/aeroelastic loads, experimental error propagation and its effects on flutter speed, a conservative value (0.3%) was cautiously considered to study stochastic flutter in Section 5.

If structural modal damping ratio equal to 0.3% is used, referring to Table 4, we observe that the SM method gives larger values of U_c in comparison with NM for all geometries and using both P and S-test data.

Using P-test data the ratio between U_c estimated with SM and NM is equal to 1.38 for MOD1, 1.11 for MOD2 and 1.28 for MOD3. The ratios are similar using S-test data. The ratio between U_c estimated with SM and NM is equal to 1.37 for MOD1, 1.20 for MOD2 and 1.27 for MOD3.

The comparison of the results for MOD2, estimated with SM and using P, S and D-test data, respectively suggests U_c ranging from 67.8 m/s (P-tests) to 104.5 m/s (D-tests). The value obtained using SM with aeroelastic data set is the highest one.

Overall, MOD3 has the highest U_c with both flutter calculation methods (NM and SM) and all experimental data (P and S). These results confirm the trend reported in Fig. 4, in which it was noted that MOD3 has smaller C_L and C_M coefficients, and consequently aerodynamic loads, in comparison with other deck sections. MOD3 often exhibits the largest absolute values of the local pressure coefficients even though this aspect does not seem to affect the U_c values.

MOD1 and MOD2 exhibit flutter results close to each other, contrary to MOD3. MOD1 leads to the smallest values of U_c using S-test data with both calculation methods (NM and SM). MOD2, on the contrary, leads to the smallest values of U_c using P-test data with both NM and SM.

5. Stochastic flutter analysis: critical speed variability and dependency on laboratory conditions

The variability of U_c values obtained with different calculation methods and different experimental data sets suggests the need to study error propagation and its effects on the U_c predictions. This aspect can be investigated by performing a comprehensive error analysis of the U_c [62] [63] [64] .

Two sample sizes of the input random variables (aerodynamic coefficients) were considered in this study, 30 and $5 \cdot 10^5$ realizations, respectively. The 30 P and S-test data sets were generated using Monte-Carlo sampling and based on the experimental results. In contrast, the 30 D-test data sets were directly deduced from the aeroelastic experiments, which were repeated 30 times (Section 2.3). Results obtained using the 30 data sets are discussed in Section 5.1.The PC expansion (e.g. [44] , [45]) using Hermite polynomials to model stochastic processes, was used to extend the size of the P, S and D-test data sets to $5 \cdot 10^5$ realizations. Results obtained using $5 \cdot 10^5$ realizations data sets are described in Section 5.2.Both flutter calculation methods (NM and SM) were used to estimate U_c with 30 samples; analyses were carried out for all geometries. The SM method and the MOD2 geometry were exclusively used for investigating U_c variability with $5 \cdot 10^5$ realizations of aerodynamic coefficients derived from P, S and D-test data sets. The probability density function (*pdf*) of the flutter speed was empirically derived from the simulations and compared against several theoretical models (Normal/Gaussian, Log-Normal, Gamma, Rayleigh and Weibull).

5.1 Critical flutter variability with 30 samples

Figs. 16, 17 and 18 illustrate the empirical probability distributions (*pdfs*) of the U_c values obtained for MOD1, MOD2 and MOD3, respectively. In particular, panel "a" of Figs. 16, 17 and 18 presents the *pdf* of U_c, evaluated by NM after processing the P-tests; panel "b" shows the *pdf* of U_c by NM after processing the S-tests; panel "c" illustrates the *pdf* of U_c calculated by SM after processing the P-tests; panel "d" shows the *pdf* of U_c calculated by SM after processing the S-tests. In addition, Figure 17e examines the empirical *pdf* graphs of U_c obtained by processing the D-test data for MOD2.

All the results indicate that the sample population (30 realizations) is rather small to obtain a continuous distribution with sufficient resolution from the corresponding empirical histograms. Consequently, the theoretical models of the *pdfs* were fitted to the experimental data and the Kolmogorov-Smirnov test was used [65] to evaluate the statistics of the results. It was found that all the models could not be rejected, at the 5% significance level, for all geometries. Thus, any of the models could not be excluded. However, the empirical fitting provides some useful information: Figs. 16, 17 and 18 suggest that the Log-Normal and Normal distributions are closer to the empirical *pdf*, with a slight preference for the Log-Normal distribution, for example for MOD1 using NM with S-test data (Fig. 16b), for MOD2 using NM with P-test (Fig. 17a) and for MOD3 using NM with S-tests (Fig. 18b). The parameters, determined through fitting of the Gamma model for all cases studied, result in a Gamma distribution very similar to the Normal and Log-Normal distribution. The Rayleigh distribution is not suitable to describe any of the cases, in particular for MOD1 using both flutter calculation methods (NM and SM) with P-tests (Figs. 16a and c), for MOD2 using SM with all experimental data sets (P, S and D-tests) (Fig. 17b, d and e) and for MOD3 using SM with the S-tests (Fig. 18d).

In conclusion, the random analyses suggest large standard deviation values. They range from 3.02 m/s to 19.78 m/s for MOD1, 6.92 m/s to 25.23 m/s for MOD2 and 2.87 m/s to 35.13 m/s for MOD3.

5.2 Critical flutter variability with $5{\cdot}10^5$ samples

This section discusses the results of the numerical analyses carried out using MOD2, SM flutter calculation method with P, S and D-test data sets synthetically expanded to obtain $5{\cdot}10^5$ realizations by PC expansions. Discussion on the PC is omitted for the sake of brevity but may be found in the literature [44] [66] [45] .

Table 5 summarizes the Hermite expansion polynomial coefficients for all *U* values discussed in section 2.3. Table 5 presents the results using Hermite polynomials with order varying from 1st to 4th . Data sets expanded using only the 3rd and 4th orders of the polynomials were used to carry out SM analyses. The P and S-test data sets were synthetically expanded using the 4th order polynomial, whereas the D-test data sets were expanded using both 3rd and 4th order polynomials. The D-test data set analyses were repeated using both correlated (i.e. with fully correlated samples of flutter derivatives) and non-correlated (i.e. independent samples of flutter derivatives) random realizations of the flutter derivatives.

Figure 19 presents the *pdfs* of the U_c with $5{\cdot}10^5$ realizations. Panel "a", shows the *pdf* of U_c evaluated with the P-test data set; panel "b" displays the *pdf* of U_c evaluated with the S-test data set; panel "c" illustrates the *pdf* of U_c calculated with non-correlated D-test data set and, finally, panel "d" shows the *pdf* of U_c calculated with correlated D-test data sets. All the probability models were fitted either to the experimental or simulated data. A Kolmogorov-Smirnov test was again performed. As previously observed with the smaller sample size, several distribution models could not be rejected at the 5% significance level.

Some information can be derived from this second investigation: the empirical or synthetic results, obtained with the P-test data sets (Fig. 19a), have an empirical probability histogram that can be adequately replicated by a Normal distribution; the graph is clearly distinct from the Rayleigh distribution. The *pdf* of U_c with the S-test data set (Fig. 19b) appears to have an empirical tri-modal distribution that is incompatible with all the *pdf* models considered. The Gamma distribution provides an acceptable approximation in terms of the mode, mean and median of the distribution (more discussion in the next section). The empirical *pdf* histograms of U_c with correlated and non-correlated D-test data sets in Figs. 19c and 19d, respectively, also exhibit a tri-modal trend that is unsuitable to any of the *pdf* models considered.

6. Additional remarks about the experimental flutter derivatives and experimental error quantification

Supplementary statistical analysis of the flutter derivatives, estimated by experimental data sets, (Section 2.3) are illustrated in Table 6. The reduced wind speed U_r equal to 7.36 is used as an example. Table 7 reports the maximum, minimum, mean $\overline{x}_\sigma$ (with x denoting any of the derivatives), standard deviation (σ) skewness (γ_3) and kurtosis (γ_4) coefficients for 30 experimental values. Table 6 also provides, in the case of the experimental data only, the standard error of the mean (S_m) defined as the ratio $\sigma/\sqrt{n_p}$, where n_p is the sample size (i.e. 30) and the relative standard deviation, i.e. the coefficient of variation (%RSD) defined as the ratio $100 \cdot \frac{\sigma}{\bar{x}_\sigma}$. The quantity S_m ranges from 0.005 to 0.2 for the experimental data; %RSD is between -56.5% (H_2^*) and +39.2% (A_1^*) for the experimental data. To provide a measure of the data set variability and examine experimental and simulation errors, the confidence (CI) and tolerance (TI) intervals were also estimated.

The confidence interval, evaluated for the experimental data sets only, measure the deviation from the true value of the mean of a random variable (unknown) and the sample mean estimator. In the present study, it was approximately estimated as $CI_{(95\%)} \approx \bar{x}_\sigma \pm 1.96\sigma/\sqrt{n_p}$, where 1.96 is the extent of the Normal/Gaussian distribution for a degree of confidence equal to 95%. This definition of $CI_{(95\%)}$ is exact if the error is normally distributed. Notoriously, the standard confidence interval equation relies on the population standard deviation (σ). However, since the latter is generally unknown, it is replaced in with the sample standard deviation. This assumption means that $CI_{(95\%)}$ is an approximation of the confidence interval, even though it is a fairly accurate approximation for large samples (i.e., $n_p \geq 30$) [67] .

The tolerance interval (TI) for each set of data, including both experimental sets and numerically-generated ones, was estimated by the algebraic sum $\bar{x}_\sigma \pm k\sigma$ (for data sets symmetric about $\bar{x}_\sigma$). The quantity k is the tolerance factor. In this study, k is defined such that there is a 99% confidence that the calculated tolerance limits will contain at least 95% of the measurements. If the normal/Gaussian distribution is employed to approximate the data variability, k=2.36 can be used.

Figures 20 and 21 present examples of tolerance and confidence intervals of the experimental flutter derivatives, estimated by repeating experiments 30 times at each U_r. At U_r = 7.36, the number of experimental data points located outside TI is equal to one only for H_1^*, A_2^* and A_3^*. The percentage of numerically-generated values, outside the TI interval, ranges from 0% (H_2^*, H_3^* and A_1^*) to 6.6% (A_2^*) (i.e. 2 points outside the interval). At U_r=14.56, the percentage of data points outside TI is equal to 3.3% for all flutter derivatives (i.e. one point outside the interval).

Finally, Table 6 provides estimation of the absolute and relative experimental errors (in percentage), referred to $\bar{x}_\sigma$ and based on the sample estimation of the TI. The two errors were defined as $\varepsilon_{TI,A} \approx 2k\sigma$ and $\varepsilon_{TI,R} \approx 2k\sigma/|\bar{x}_\sigma|$, respectively, and depend on U_r. For example, $\varepsilon_{TI,R}$ varies from 51.2% (A_3^*) and 268.7% (H_2^*) at U_r=7.36. This supplementary analysis confirms the variability of the flutter derivatives that is reflected in the critical flutter speed estimation.

7. Further discussion of the stochastic flutter results

Numerical simulation results (Table 7) indicate that the variability of critical flutter speed, obtained using the various calculation methods and the experimental data sets, is large. For example, in the case of the MOD2 deck section, the critical flutter speed shown was calculated using both NM and SM and the three different experimental data sets (P, S and D-tests).

The mean and standard deviation of the flutter speed U_c are presented. The lowest and the highest values of U_c were obtained by evaluating flutter speed using one sample of experimental data: they are equal to 60.75 m/s (NM combined with P-test data sets) and 104.50 m/s (SM with D-test data sets). When 30 repeated realizations of the experimental data were employed, the smallest mean value of U_c, equal to 66.76 m/s, was found by NM with S-test data sets; the standard deviation was determined as 6.92 m/s. The largest mean value of U_c, equal to 91.10 m/s, was obtained using SM with D-test data sets; the standard deviation was 29.21 m/s. Finally, when the $5 \cdot 10^5$ synthetic realizations were processed, the lowest mean value of U_c, 71.48 m/s, was estimated using SM with the P-test data set synthetically expanded with a 4th order Hermite-polynomial PC; the standard deviation was equal to 13.28. In contrast, the largest mean value, 96.70 m/s, was obtained using SM with an S-test data set expanded with a 4th order PC. The maximum value of standard deviation was observed when SM was utilized with a D-test data set expanded with a 4th order Hermite-polynomial PC and non-correlated flutter derivatives. In conclusion, the ratio between the lowest and the highest value of evaluated can be large, equal to about 1.72.

8. Conclusions

Experimental error propagation, associated with variability in the aerodynamic loads of bridge decks, has considerable impact on the critical flutter speed of pedestrian suspension bridges. In this paper a comprehensive investigation was carried out to examine the implications of this kind of variability on the structural reliability of such bridges. Three different experimental data sets were considered: pressure coefficients (P-test data set), aerodynamic static forces (S-test data set) and flutter derivatives (d-test data set). The data sets were measured in three different laboratories, CRIACIV Boundary Layer Wind Tunnel (Prato, Italy), Marche Polytechnic University's wind tunnel (Ancona, Italy) and Northeastern University's wind tunnel (Boston, Massachusetts, USA). The study was applied to three different pedestrian suspension bridges with closed-box deck sections of various geometries (MOD1, MOD2 and MOD3).

The critical flutter speed was estimated by three-dimensional finite-element nonlinear dynamic analysis (NM) and frequency-domain equivalent 2-DOF analysis (SM). Due to the small number of experimental samples, synthetic generation of a larger data sample was needed to conduct the stochastic flutter analysis. Monte-Carlo simulation methods and spectral methods, based on

Polynomial Chaos expansion of random variables using Hermite polynomials, were considered. Table 6 presents the analysis of experimental and numerical flutter derivative data sets along with empirical tolerance and confidence intervals. Table 7 summarizes the main results. Results suggest that different calculation methods and different experimental data sets influence estimations of critical flutter speed. Careful attention should be paid to these aspects especially in the case of pedestrian footbridges, for the design of which comprehensive aerodynamic and aeroelastic investigations are not always prescribed and may not be carried out.

Acknowledgments

The authors would like to gratefully acknowledge Dr. Federica Speziale for her collaboration with the experiments and for sharing the data of her PhD dissertation. Professor Piero D'Asdia, University of Chieti-Pescara "G. D'Annunzio", Italy, is acknowledged for providing the initial motivation for this project. We thank Professor Renato Ricci for his contributions and collaboration during the experiments in the wind tunnel of the Marche Polytechnic University, Italy. The authors also acknowledge Professor Jerome F. Hajjar, the Departments of Civil/Environmental Engineering and Mechanical/Industrial Engineering of Northeastern University for collaboration with sensor equipment and the experiments carried out in the Northeastern University's wind tunnel. Finally, Messrs. Kurt Braun and Michael MacNeil are gratefully acknowledged for the collaboration with the experimental setup and the tests at Northeastern University.

References

[1] Tondini N, Bonelli A, Bursi OS, Francescotti S. Dynamic and aeroelastic behavior of a twin deck curved cable-stayed footbridge equipped with passive devices. In: Proceedings of EURODYN 2011, Eighth International Conference on Structural Dynamics, Leuven, Belgium; 2011.

[2] Gimsing NJ, Georgakis CT. Cable Supported Bridges: Concept and Design, Third Edition. Wiley, Chichester, United Kingdom; 2011.

[3] Strasky J. Stress ribbon and cable-supported pedestrian bridges. London, United Kingdom: Thomas Telford, Heron Quay; 2005

[4] Blekherman AN. Swaying of Pedestrian Bridges, Journal of Bridge Engineering 2005;10(2):142-50

[5] Blekherman AN, Internal resonance in pedestrian bridges. International Journal of Bridge Engineering 2015;3(3):1-33.

[6] Fujino Y, Pacheco BM, Nakamura SI, Warnitchai P. Synchronization of human walking observed during lateral vibration of a congested pedestrian bridge. Earthquake Engineering & Structural Dynamics 1993;22(9):741–58.

[7] Huang MH, Thambiratnam DP, Perera NJ. Dynamic performance of slender suspension footbridges under eccentric walking dynamic loads. Journal of Sound and Vibration 2007;303(1-2):239-54.

[8] Ingólfsson ET. Pedestrian-induced lateral vibrations of footbridges: Experimental studies and probabilistic modelling", Ph.D. Thesis, Department of Civil Engineering Technical University of Denmark; 2011.

[9] Ingólfsson ET, Georgakis CT, Jönsson J. Pedestrian-induced lateral vibrations of footbridges: A literature review. Engineering Structures 2012; 45:21-52.

[10] Rehmanjee Y H. Lateral Vibration of Pedestrian Bridges. MS Thesis. Boston, Massachusetts, USA: Massachusetts Institute of Technology, Department of Civil and Environmental Engineering; 2000.

[11] Ricciardelli F, Hangan H. Pressure distribution and aerodynamic forces on stationary box bridge sections". Wind and Structures 2001;4:399-412.

[12] Ricciardelli F, de Grenet ET, Hangan H. Pressure distribution, aerodynamic forces and dynamic response of box bridge sections. Journal of Wind Engineering & Industrial Aerodynamics 2002;90(10):1135-50.

[13] Roberts T. M., 2005. "Lateral Pedestrian Excitation of Footbridges", *Journal of Bridge Engineering*, 10(1).

[14] Tubino F. Relationships among aerodynamic admittance functions flutter derivatives and static coefficients for long-span bridges. Journal of Wind Engineering and Industrial Aerodynamics 2005;93(12):929-50.

[15] Tubino F, Solari G. Gust buffeting of long span bridges: double modal transformation and effective turbulence. Engineering Structures 2007;29(8):1698-707.

[16] Zasso A, Stoyanoff S, Diana G, Vullo E, Khazem D, Serzan K et al. Validation analyses of integrated procedures for evaluation of stability, buffeting response and wind loads on the Messina bridge. Journal of Wind Engineering and Industrial Aerodynamics 2013;122:50–9.

[17] Pourzeynali S, Datta TK. Reliability analysis of suspension bridges against flutter. Journal of Sound Vibration 2002;254:143–162.

[18] Ge YJ, Xiang HF, Tanaka H. Application of a reliability analysis model to bridge flutter under extreme winds. Journal of Wind Engineering and Industrial Aerodynamics 2000;86:155–67.

[19] Cheng J, Cai CS, Xiao RC, Chen SR. Flutter reliability analysis of suspension bridges. Journal of Wind Engineering and Industrial Aerodynamics 2005;93:757–75.

[20] Baldomir A, Hernández S, Nieto F, Jurado J. Reliability analysis of flutter speed in long span bridges using form technique. In: Proceedings of the Thirteenth International Conference on Wind Engineering (ICWE 13), Amsterdam, NL; 2013.

[21] Baldomir A, Kusano I, Jurado JA, Hernández S. A reliability study for the Messina Bridge with respect to flutter phenomena considering uncertainties in experimental and numerical data. Computers and Structures 2013;128:91-100.

[22] Sarkar PP, Caracoglia L, Haan FL, Sato H, Murakoshi J. Comparative and sensitivity study of flutter derivatives of selected bridge deck sections. Part 1: Analysis of inter-laboratory experimental data. Engineering Structures 2009;31(1):158-69.

[23] Scanlan RH, Tomko JJ. Airfoil and bridge deck flutter derivatives". Journal of Engineering Mechanics, ASCE 1971;97(EM6):1717-37.

[24] Argentini T, Belloli M, Fossati F, Rocchi D, Villani M. Experimental and numerical analysis of the dynamic response of cable-stayed bridge: vortex induced vibrations and buffeting effects. In: Proceedings of the 13th International Conference on Wind Engineering. IAWE, Amsterdam, Netherlands; 2011.

[25] Diana G, Fiammenghi G, Belloli M, Rocchi D. Wind tunnel tests and numerical approach for long span bridges: The Messina bridge. Journal of Wind Engineering and Industrial Aerodynamics 2013;122:38-49.

[26] Diana G, Falco M, Bruni S Cigada A, Larose G, Damsgaard A, Collina A. Comparisons between wind tunnel tests on a full aeroelastic model of the proposed bridge over Stretto di Messina and numerical results. Journal of Wind Engineering and Industrial Aerodynamics 1995;54–55:101–13.

[27] Argentini T, Diana G, Larsen A, Pagani A, Portentoso M, Somaschini C, Yamasaki Y. Comparisons between wind tunnel tests on a full aeroelastic model and numerical results of the Izmit bay bridge. In: Proceedings of the 6th European African Conference on Wind Engineering, Cambridge UK; 2013.

[28] Scanlan, RH, Jones NP, Singh L. Inter-relations among flutter derivatives. Journal of Wind Engineering and Industrial Aerodynamics 1997;69-71:829-37.

[29] Matsumoto M, Kobayashi Y, Shirato H. The influence of aerodynamic derivatives on flutter. Journal of Wind Engineering and Industrial Aerodynamics 1996;60:227–39.

[30] Lau CK, Wong KY. Aerodynamic stability of Tsing Ma Bridge. In: Proceedings of the Fourth International Kerensky Conference on Structures in the New Millennium, Hong Kong; 1997.

[31] Zdravkovich MM, Carelas E. Aerodynamics of a covered pedestrian bridge of a trapezoidal section. Journal of Wind Engineering and Industrial Aerodynamics 1995;66:141-53.

[32] Zhanga XJ, Sun BN. Parametric study on the aerodynamic stability of a long-span suspension bridge. Journal of Wind Engineering and Industrial Aerodynamics 2004;92(6),431–39.

[33] Jones NP, Scanlan RH. Theory and full-bridge modeling of wind response of cable-supported bridges. Journal of Bridge Engineering, ASCE, 2001; (6):365-75.

[34] Speziale F. Aerodynamic and aeroelastic response of streamlined single box sections for long-span bridge decks. PhD Dissertation. Pescara, Italy: University of Pescara; 2015.

[35] Jakobsen JB, Tanaka H. Modelling uncertainties in prediction of aeroelastic bridge behaviour. Journal of Wind Engineering and Industrial Aerodynamics 2003;91:1485–98.

[36] Prenninger PHW, Matsumoto M, Shiraishi N, Izumi C, Tsukiyama Y. Reliability of bridge structures under wind loading. Consideration of uncertainties of wind load parameters. Journal of Wind Engineering and Industrial Aerodynamics 1990;33:385–94.

[37] Bartoli G, Mannini C. Reliability of bridge deck flutter derivative measurement in wind tunnel tests. In: Proceedings of ICOSSAR 2005 Conference; 2005.

[38] Barlow JB, Rae WH, Pope A. Low-speed wind tunnel testing, (third edition), John Wiley and sons, New York, New York, USA; 1999.

[39] Belloli M, Fossati F, Giappino S, Muggiasca S. Vortex induced vibrations of a bridge deck: Dynamic response and surface pressure distribution. Journal of Wind Engineering & Industrial Aerodynamics 2014;133:160-68.

[40] Simiu E Scanlan RH. Wind Effects on Structures: Fundamentals and Applications to Design, 3rd edition. New York, USA: John Wiley and Sons; 1996.

[41] Singh L. Experimental determination of aeroelastic and aerodynamic parameters of long-span bridges. PhD Dissertation. Baltimore, Maryland, USA: Johns Hopkins University; 1997.

[42] Argentini T, Pagani A, Rocchi D, Zasso A. Monte Carlo analysis of total damping and flutter speed of a long span bridge: Effects of structural and aerodynamic uncertainties. Journal of Wind Engineering and Industrial Aerodynamics 2014;128:90-104.

[43] Zio E, Marseguerra M. Basics of the Monte Carlo method with application to system reliability. London, UK: Springer-Verlag; 2002.

[44] Ghanem R, Spanos PD. Stochastic finite elements: a spectral approach. Springer-Verlag, New York, New York, USA; 1991.

[45] Xiu D, Karniadakis GE. The Wiener-Askey polynomial chaos for stochastic differential equations. SIAM Journal on Scientific Computing 2002;24(2):619-44.

[46] Ostenfeld-Rosenthal P, Madsen HO, Larsen A. Probabilistic flutter criteria for long span bridges. Journal of Wind Engineering and Industrial Aerodynamics 1992;42:1265–76.

[47] Taylor IJ, Vezza M, Salisbury I. Numerical investigation of the effects of pedestrian barriers on aeroelastic stability of a proposed footbridge. Journal of Wind Engineering and Industrial Aerodynamics 2008;96(12):2418-37.

[48] Scanlan, RH, Jones NP. Aeroelastic analysis of cable-stayed bridges. Journal of Structural Engineering, ASCE 1990;116(2):279-97.

[49] Augusti G, Spinelli P, Borri C, Bartoli G, Giachi M, Giordano S. The C.R.I.A.C.I.V. Atmospheric Boundary Layer Wind Tunnel. In: Proceeding of the 9th International Conference on Wind Engineering, New Delhi. Wiley Eastern Ltd; 1995.

[50] Scotta R, Lazzari M, Stecca E, Cotela J, Rossi R. Numerical wind tunnel for aerodynamic and aeroelastic characterization of bridge deck sections. Computers and Structures 2016;167:96–114.

[51] Reinhold TA, Brinch M, Damsgaard A. Wind tunnel tests for the Great Belt Link. In: Larsen A, editor. Aerodynamics of Large Bridges - Proceedings of the 1st International Symposium on Aerodynamics of Large Bridges (Copenhagen, Denmark, 1992). Rotterdam, NL: Balkema, ISBN 905410 042 7; 1992: p. 255-67.

[52] Katsuchi H, Jones N P, Scanlan RH. Multimode coupled buffeting and flutter analysis of the Akashi-Kaikyo Bridge. Journal of Structural Engineering, ASCE 1999;125(1):60-70.

[53] Brito R, Caracoglia L. Extraction of flutter derivatives from small scale wind tunnel experiments. In: Proceedings of the 11th Americas Conference on Wind Engineering, American Association for Wind Engineering (AAWE), San Juan, Puerto Rico; 2009.

[54] Rizzo F, Caracoglia L. Examination of experimental errors in Scanlan derivatives of a closed-box bridge deck. Wind and Structures, An International Journal, 2018:26(4):231-251.

[55] Chowdhury AG, Sarkar PP. A new technique for identification of eighteen flutter derivatives using a three-degree-of-freedom section model. Engineering Structures 2003;25(12):1763–72.

[56] Kwon SD. Uncertainty of bridge flutter velocity measured at wind tunnel tests. In Proceedings of the 5th International Symposium on Computational Wind Engineering (CWE2010), Chapel Hill, North Carolina, USA; 2010.

[57] Buljac A, Kozmar H, Pospíšil S, Macháček M, Král R. Dynamic stability of the Golden Gate Bridge deteriorated by roadway wind barriers". In: Proceedings of the 8th International Symposium BBAA VIII, Northeastern University, paper ID 109 (electronic proceedings); 2016.

[58] CEN (Comité Européen de Normalization). Eurocode 1: Actions on structures - Part 1-4: General actions - Wind actions, EN-1991-1-4; 2005.

[59] Tveiten J. Dynamic analysis of a suspension bridge. MS Thesis. Stavanger, Norway: University of Stavanger, Structural Engineering. University of; 2012.

[60] Xiang HF, Ge YJ. Refinements on aerodynamic stability analysis of super long-span bridges. Journal of Wind Engineering and Industrial Aerodynamics 2002;90:1493–515.

[61] Gordon S. Critical analysis of the first Severn Bridge. In: Proceedings of Bridge Engineering 2 Conference, Bath, United Kingdom; 2010.

[62] Mannini C, Bartoli G. A probabilistic approach to bridge deck flutter. In: Proceedings of the Twelfth International Conference on Wind Engineering (ICWE12), Cairns, Australia; 2007.

[63] Mannini C, Bartoli G. The problem of uncertainty in the measurement of aerodynamic derivatives. In: Safety, Reliability and Risk of Structures, Infrastructures and Engineering Systems, Proceedings 10th International Conference on Structural Safety and Reliability, Osaka, Japan; 2010: p. 824–31.

[64] Seo DW, Caracoglia L. Statistical buffeting response of flexible bridges influenced by errors in aeroelastic loading estimation. Journal of Wind Engineering and Industrial Aerodynamics 2012;104-106:129-40.

[65] Massey FJ. The Kolmogorov-Smirnov test for goodness of fit. Journal of the American Statistical Association 1951;46(253):68-78.

[66] Le Maître O.P. and Knio O.M., 2010, "Spectral methods for uncertainty quantification", Springer, Dordrecht, Heidelberg, London, New York.

[67] Walpole R, Myers R, Myers S, Ye K. Probability and statistics for engineers and scientists. 9th edition. Upper Saddle River, NJ, USA: Pearson - Prentice Hall; 2002.

List of Tables:

Table 1

		h_1	h_2	d_1	b_1	d_2	b_2
Full scale	MOD1	$0.53 \cdot 10^3$	$1.11 \cdot 10^3$	$0.86 \cdot 10^3$	$10.25 \cdot 10^3$	$4.10 \cdot 10^3$	$3.94 \cdot 10^3$
	MOD2	$0.53 \cdot 10^3$	$1.11 \cdot 10^3$	$0.86 \cdot 10^3$	$10.25 \cdot 10^3$	$2.62 \cdot 10^3$	$6.77 \cdot 10^3$
	MOD3	$0.53 \cdot 10^3$	$1.11 \cdot 10^3$	$0.86 \cdot 10^3$	$10.25 \cdot 10^3$	$1.89 \cdot 10^3$	$8.36 \cdot 10^3$
Wind tunnel model							
S and P-tests	MOD1	13	27	21	250	100	96
	MOD2	13	27	21	250	64	165
	MOD3	13	27	21	250	46	204
D-tests	MOD1	-	-	-	-	-	-
	MOD2	7	14	11	127	32	84
	MOD3	-	-	-	-	-	-

Notes: all values are in mm; the definition of the quantities refers to Fig. 2.

Table 2

Models	ϕ	s	I_x	J_g	F	A_h	$\varepsilon_{h,0}$	A_c	$\varepsilon_{c,0}$
	m	m	m^4	m^4	kN/m	m^2	%	m^2	%
MOD1	$1.\cdot10^{-2}$	$4\cdot10^{-3}$	$2.7\cdot10^{-3}$	$1.2\cdot10^{-2}$	4.96	$7.07\cdot10^{-4}$	0.70	$1.54\cdot10^{-2}$	0.51
MOD2	$1.\cdot10^{-2}$	$5\cdot10^{-3}$	$3.7\cdot10^{-3}$	$1.7\cdot10^{-2}$	6.26	$7.07\cdot10^{-4}$	0.70	$1.54\cdot10^{-2}$	0.52
MOD3	$1.\cdot10^{-2}$	$6\cdot10^{-3}$	$5.6\cdot10^{-3}$	$2.3\cdot10^{-2}$	7.45	$7.07\cdot10^{-4}$	0.70	$1.54\cdot10^{-2}$	0.53

Table 3

Models	*Natural frequencies*					
	1th symmetric vertical ($\omega_{h,1}/2\pi$) (Hz)	*1th symmetric torsional($\omega_{\alpha,1}/2\pi$) (Hz)*	*1th asymmetric vertical ($\omega_{h,2}/2\pi$) (Hz)*	*1th asymmetric torsional ($\omega_{\alpha,2}/2\pi$) (Hz)*	$\frac{\omega_{\alpha,1}}{\omega_{h,1}}$	$\frac{\omega_{\alpha,2}}{\omega_{h,2}}$
MOD1	0.40 mode 12^{th}	0.57 mode 14^{th}	0.26 mode 5^{th}	0.58 mode 15^{th}	1.42	2.23
MOD2	0.35 mode 8^{th}	0.57 mode 15^{th}	0.25 mode 5^{th}	0.56 mode 14^{th}	1.62	2.24
MOD3	0.34 mode 8^{th}	0.56 mode 14^{th}	0.33 mode 7^{th}	0.55 mode 13^{th}	1.64	1.66

Table 4

Data set	Model	Calculation method	Damping ratio, ξ (%) 0.1	0.2	0.3	0.4	0.5
			U_c (m/s)				
P-tests	MOD1	NM	24.3	37.0	61.6	90.5	90.7
		SM	37.7	39.6	85.1	91.2	92.9
	MOD2	NM	22.1	41.5	60.9	101.4	103.5
		SM	23.7	42.4	67.8	113.1	113.2
	MOD3	NM	25.8	86.8	107.4	110.2	112.9
		SM	31.8	88.0	138.3	187.2	186.9
S-tests	MOD1	NM	25.2	33.8	52.4	90.5	91.4
		SM	27.0	34.0	72.0	114.0	118.0
	MOD2	NM	25.8	36.6	65.8	82.30	83.1
		SM	32.8	46.9	79.8	113.9	115.1
	MOD3	NM	29.0	73.0	129.0	131.0	132.0
		SM	36.0	98.4	164.2	190.6	192.0
D-tests	MOD1	NM	-	-	-	-	-
		SM	-	-	-	-	-
	MOD2	NM	-	-	-	-	-
		SM	43.0	61.5	104.5	130.6	131.9
	MOD3	NM	-	-	-	-	-
		SM	-	-	-	-	-

Table 5

	Hermite expansion polynomial order	Reduced wind speed, U_r (m/s)							
		3.27	4.57	5.86	7.36	9.18	10.85	12.88	14.56
H_1*	1st Ord.	0.45	0.39	0.57	0.73	0.74	1.36	2.53	2.67
	2nd Ord.	0.45	0.39	0.57	0.73	0.74	1.36	2.53	2.67
	3rd Ord.	0.45	0.39	0.57	0.74	0.74	1.36	2.53	2.67
	4th Ord.	0.45	0.39	0.57	0.72	0.74	1.36	2.54	2.67
H_2*	1st Ord.	0.55	0.53	0.53	0.53	0.56	0.63	0.73	1.15
	2nd Ord.	0.55	0.53	0.53	0.53	0.56	0.63	0.73	1.15
	3rd Ord.	0.55	0.53	0.53	0.53	0.56	0.63	0.73	1.15
	4th Ord.	0.55	0.53	0.53	0.53	0.56	0.63	0.73	1.15
H_3*	1st Ord.	0.37	0.28	0.27	0.29	0.33	0.36	0.43	0.95
	2nd Ord.	0.37	0.27	0.27	0.29	0.33	0.36	0.43	0.95
	3rd Ord.	0.37	0.27	0.27	0.29	0.32	0.36	0.43	0.95
	4th Ord.	0.37	0.27	0.27	0.29	0.33	0.36	0.43	0.96
A_1*	1st Ord.	0.89	0.56	0.56	1.10	1.89	2.60	2.59	2.84
	2nd Ord.	0.89	0.56	0.56	1.10	1.89	2.60	2.59	2.84
	3rd Ord.	0.89	0.56	0.56	1.10	1.89	2.59	2.59	2.84
	4th Ord.	0.89	0.56	0.56	1.10	1.90	2.59	2.59	2.84
A_2*	1st Ord.	0.04	0.01	0.01	0.03	0.09	0.11	0.15	0.31
	2nd Ord.	0.04	0.01	0.01	0.03	0.09	0.11	0.15	0.31
	3rd Ord.	0.04	0.01	0.01	0.03	0.09	0.11	0.15	0.31
	4th Ord.	0.04	0.01	0.01	0.03	0.09	0.11	0.15	0.31
A_3*	1st Ord.	0.15	0.10	0.10	0.10	0.12	0.13	0.17	0.34
	2nd Ord.	0.15	0.10	0.10	0.10	0.12	0.13	0.17	0.34
	3rd Ord.	0.15	0.10	0.10	0.10	0.12	0.13	0.17	0.34
	4th Ord.	0.15	0.10	0.10	0.10	0.12	0.13	0.17	0.34

Table 6

	Data source	max	min	$\overline{x}_{\sigma}$	s	γ_3	γ_4	S_m	%RSD	TI		$CI_{(95\%)}$		ε_{TI}	$\varepsilon_{CI(95\%)}$
H_1^*	Exp.	-3.24	-6.49	-5.04	0.73	0.17	3.02	0.134	-14.5	-3.31	-6.77	-4.78	-5.30	68.6	10.4
	3rd HP	12.28	-18.50	-5.04	0.73	0.08	1.85	0.001	-14.5						
	4th HP	52.72	-5.89	-5.04	0.74	0.08	1.54	0.001	-14.7						
H_2^*	Exp.	0.16	-2.02	-0.94	0.53	0.14	2.76	0.097	-56.5	0.31	-2.19	-0.75	-1.13	266.5	40.4
	3rd HP	9.20	-16.77	-0.94	0.53	-0.92	2.93	0.001	-56.5						
	4th HP	53.80	-2.20	-0.94	0.53	1.17	3.70	0.001	-56.9						
H_3^*	Exp.	2.20	1.06	1.57	0.29	0.08	2.61	0.053	18.5	2.26	0.89	1.67	1.47	87.2	13.2
	3rd HP	4.75	-0.35	1.57	0.29	1.03	2.80	0.001	18.5						
	4th HP	4.29	-36.80	2.81	1.10	0.48	1.59	0.001	39.3						
A_1^*	Exp.	4.43	0.74	2.81	1.10	-0.32	2.01	0.201	39.2	5.41	0.21	3.21	2.42	185.2	28.1
	3rd HP	4.20	-5.55	2.81	1.10	1.53	4.35	0.001	39.3						
	4th HP	10.92	0.86	1.57	0.29	0.23	1.66	0.001	18.5						
A_2^*	Exp.	-0.01	-0.13	-0.06	3.E-02	-0.55	3.25	0.005	-51.9	0.01	-0.13	-0.05	-0.07	245.3	37.2
	3rd HP	0.64	-0.54	-0.06	3.E-02	-1.32	3.21	0.001	-52.2						
	4th HP	-0.01	-2.87	-0.06	3.E-02	-1.36	3.17	0.001	-52.8						
A_3^*	Exp.	1.13	0.67	0.91	1.E-01	0.11	3.18	0.018	10.9	1.14	0.68	0.94	0.87	51.2	7.8
	3rd HP	3.57	-1.52	0.91	1.E-01	0.82	2.45	0.001	10.9						
	4th HP	1.09	-4.54	0.91	1.E-01	0.91	2.70	0.001	10.9						

Note: 3rd HP and 4th HP refer to 3rd and 4th order of Hermite polynomials.

Table 7

MOD2 (ξ=0.3%)		U_c (m/s)				
Data set	Calculation method	**Single realization**	**30 realizations** $\overline{U_c}$	σ_{U_c}	**510e5 realizations** $\overline{U_c}$	σ_{U_c}
P-tests	NM	60.75	68.23	23.72	-	-
	SM	67.84(#)	70.63	14.84(#)	4^{th} order 71.48	4^{th} order 13.28(#)
S-tests	NM	65.80	66.76	6.92	-	-
	SM	79.76(#)	89.22	20.88(#)	4^{th} order 96.70	4^{th} order 35.49(#)
D-tests	NM	-	-	-	-	-
	SM	104.5	91.12	29.21	Non-correlated 3^{rd} order 83.57 4^{th} order 87.37 Correlated 4^{th} order 95.25	 3^{rd} order 36.66 4^{th} order 37.56 4^{th} order 26.85

(ξ=0.3%)		ω_c (rad/s)		
Data set	Calculation Method	**Single realization**	**30 realizations** $\overline{U_c}$	**$5\cdot10^5$ realizations** $\overline{U_c}$
P-tests	NM	0.217	0.193	-
	SM	0.194(#)	0.186	4^{th} order 0.184
S-tests	NM	0.200	0.197	-
	SM	0.165(#)	0.147	4^{th} order 0.136
D-tests	NM	-	-	-
	SM	0.126	0.144	Non-correlated 3^{rd} order 0.157 4^{th} order 0.150 Correlated 4^{th} order 0.138

Note (#): quasi-static approximation of flutter derivatives (Scanlan et al. 1997)

List of Figures:

Figure 17: MOD2, empirical *pdf* graphs with 30 realizations: NM/P-tests (a), NM/S-tests (b), SM/P-tests (c), SM-S-tests (d) and (e) SM-D-tests

Figure 18: MOD3, empirical *pdf* graphs with 30 realizations: NM/P-tests (a), NM/S-tests (b), SM/P-tests (c), SM-S-tests (d).

Figure 19: MOD2, empirical *pdf* graphs with $5 \cdot 10^5$ realizations, SM/P-tests (a), SM/S-tests (b), SM/D-tests (uncorrelated flutter derivatives) (c), SM/D-tests (correlated flutter derivatives) (d).

Figure 20: MOD2, analysis of experimental datasets, tolerance (TI) and confidence intervals (CI) of H_1^* at reduced wind speeds U_r=7.36 (a) and U_r=14.56 (b); H_2^* at U_r=7.36 (c) and U_r=14.56 (d); H_3^* at U_r=7.36 (e) and U_r=14.56 (f).

Figure 21: MOD2, analysis of experimental datasets, tolerance (TI) and confidence intervals (CI) of A_1^* at reduced wind speeds U_r=7.36 (a) and U_r=14.56 (b); A_2^* at U_r=7.36 (c) and U_r=14.56 (d); A_3^* at U_r=7.36 (e) and U_r=14.56 (f).

(a) (b)

Figure 1

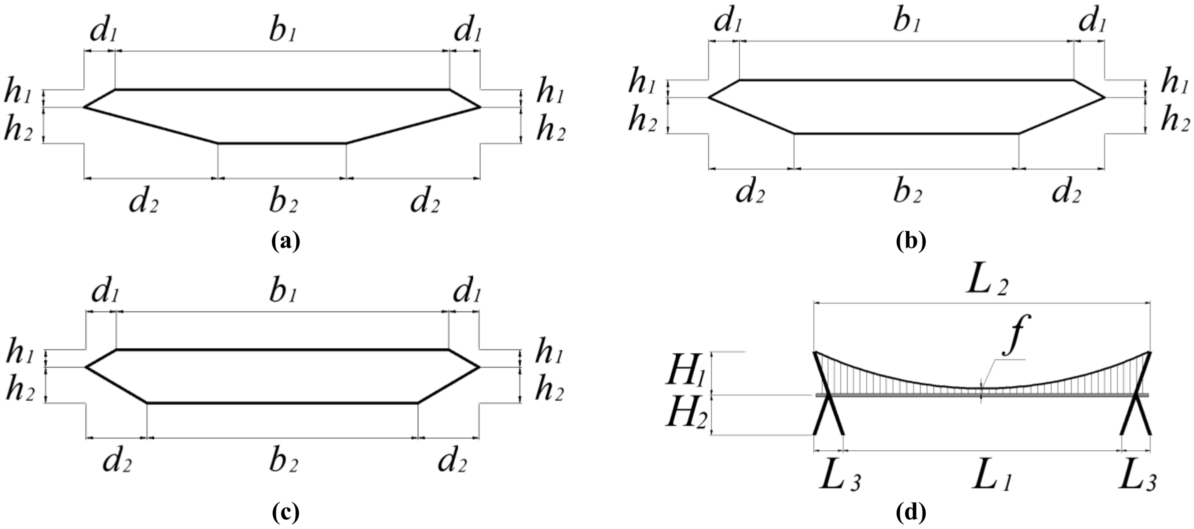

Figure 2

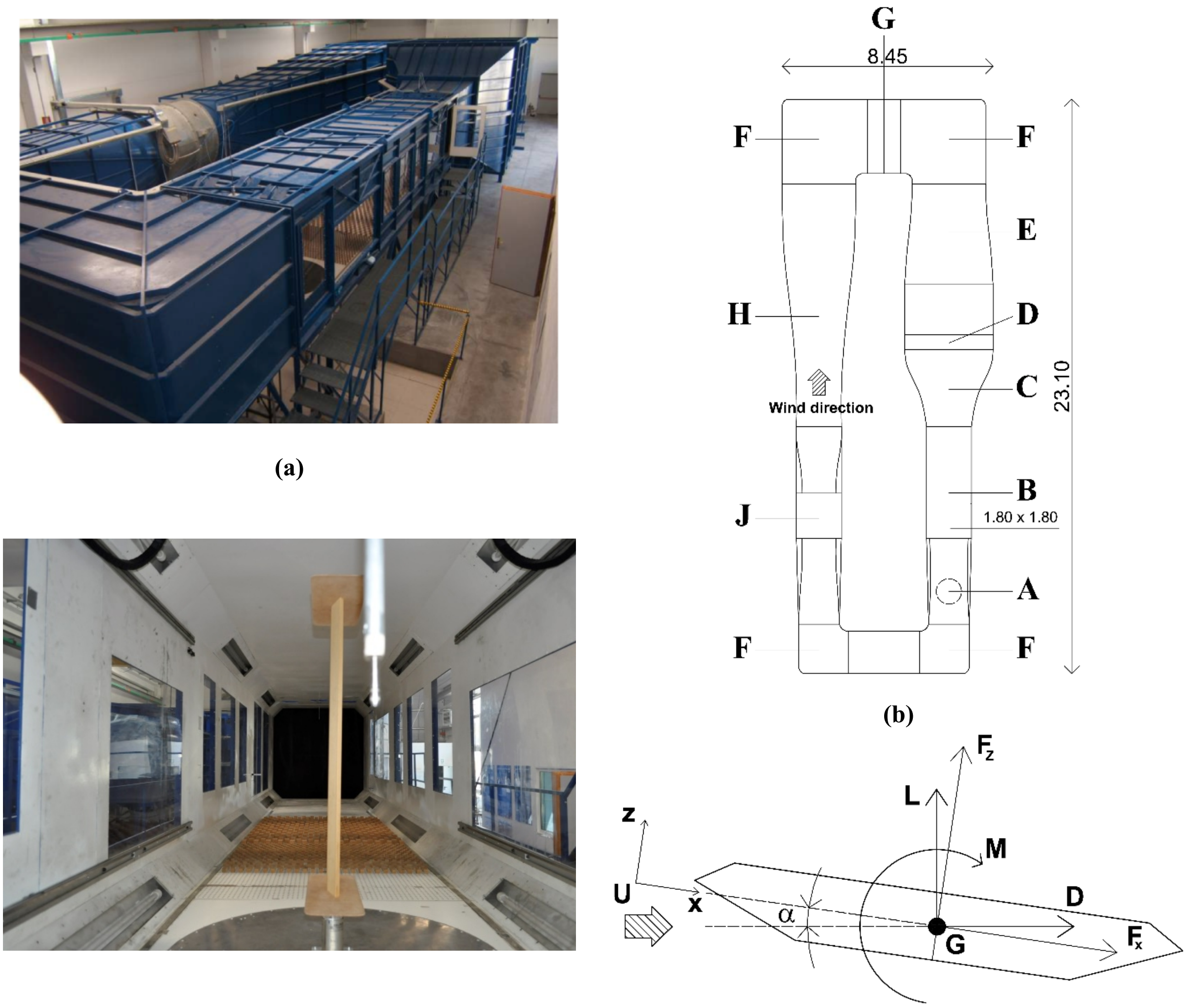

(a) (b) (c) (d)

Figure 3

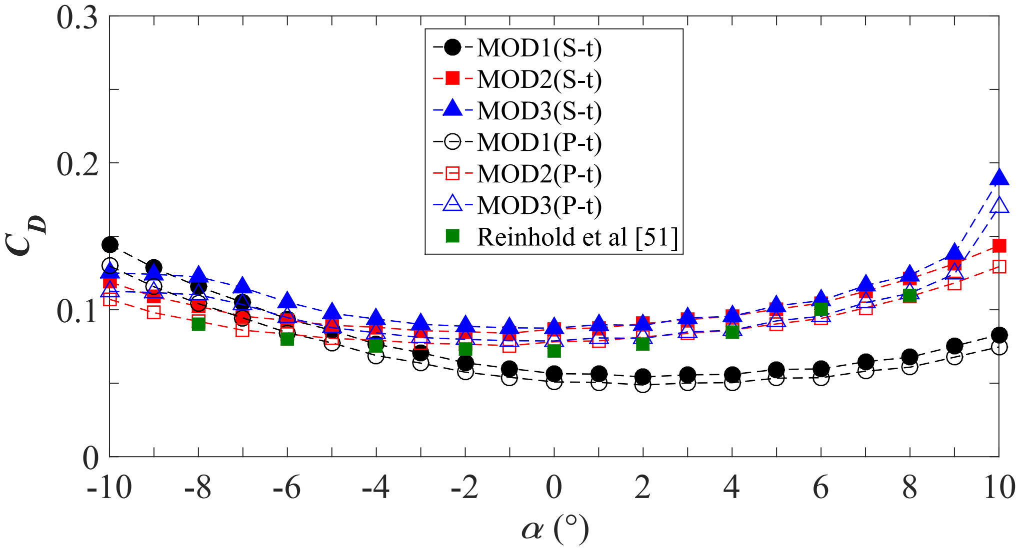

MOD1(S-t)
MOD2(S-t)
MOD3(S-t)
MOD1(P-t)
MOD2(P-t)
MOD3(P-t)
Reinhold et al [51]
C_D
α (°)

(a)

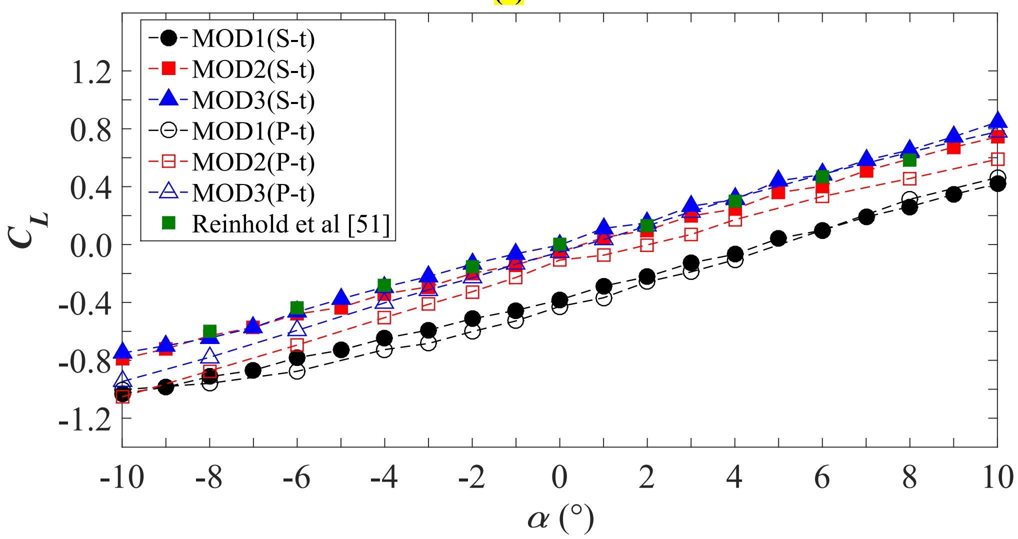

MOD1(S-t)
MOD2(S-t)
MOD3(S-t)
MOD1(P-t)
MOD2(P-t)
MOD3(P-t)
Reinhold et al [51]
C_L
α (°)

(b)

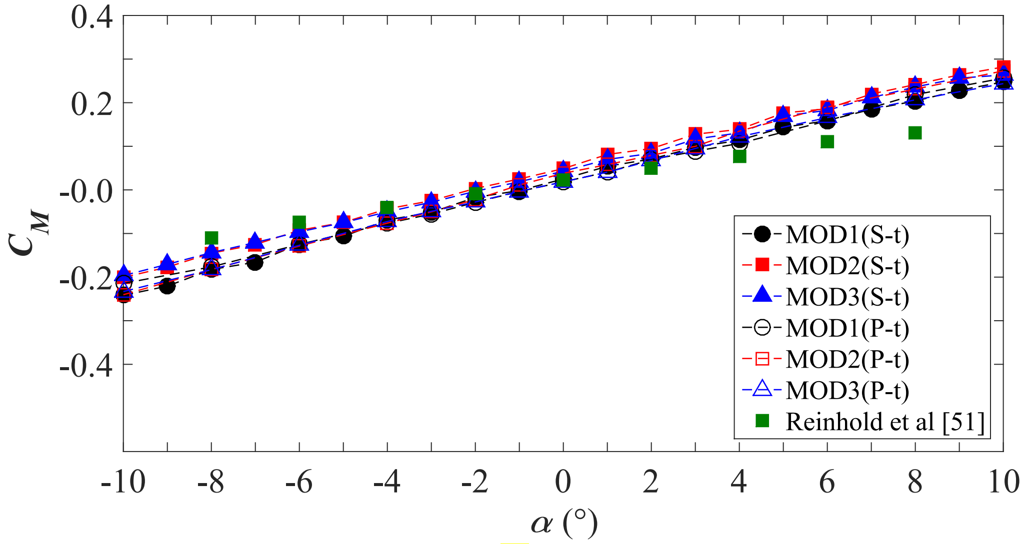

MOD1(S-t)
MOD2(S-t)
MOD3(S-t)
MOD1(P-t)
MOD2(P-t)
MOD3(P-t)
Reinhold et al [51]
C_M
α (°)

(c)

Figure 4

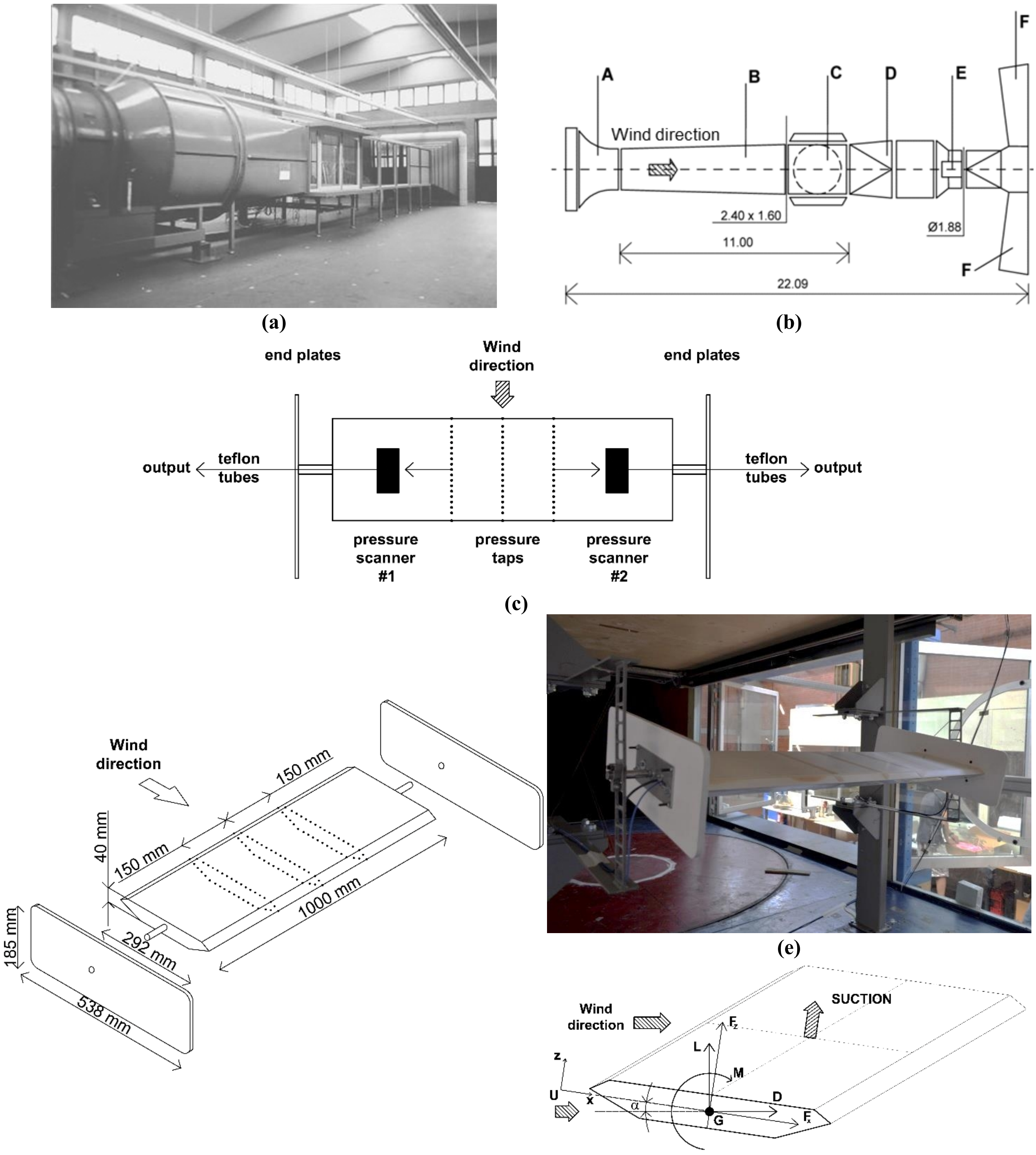
(a)
A
B
C
D
E
F
Wind direction
2.40 x 1.60
11.00
Ø1.88
22.09
(b)
end plates
Wind direction
end plates
output
teflon tubes
pressure scanner #1
pressure taps
pressure scanner #2
(c)
Wind direction
150 mm
150 mm
40 mm
1000 mm
292 mm
185 mm
538 mm
(d)
(e)
Wind direction
SUCTION
z
x
U
L
M
D
G
α
(f)

Figure 5

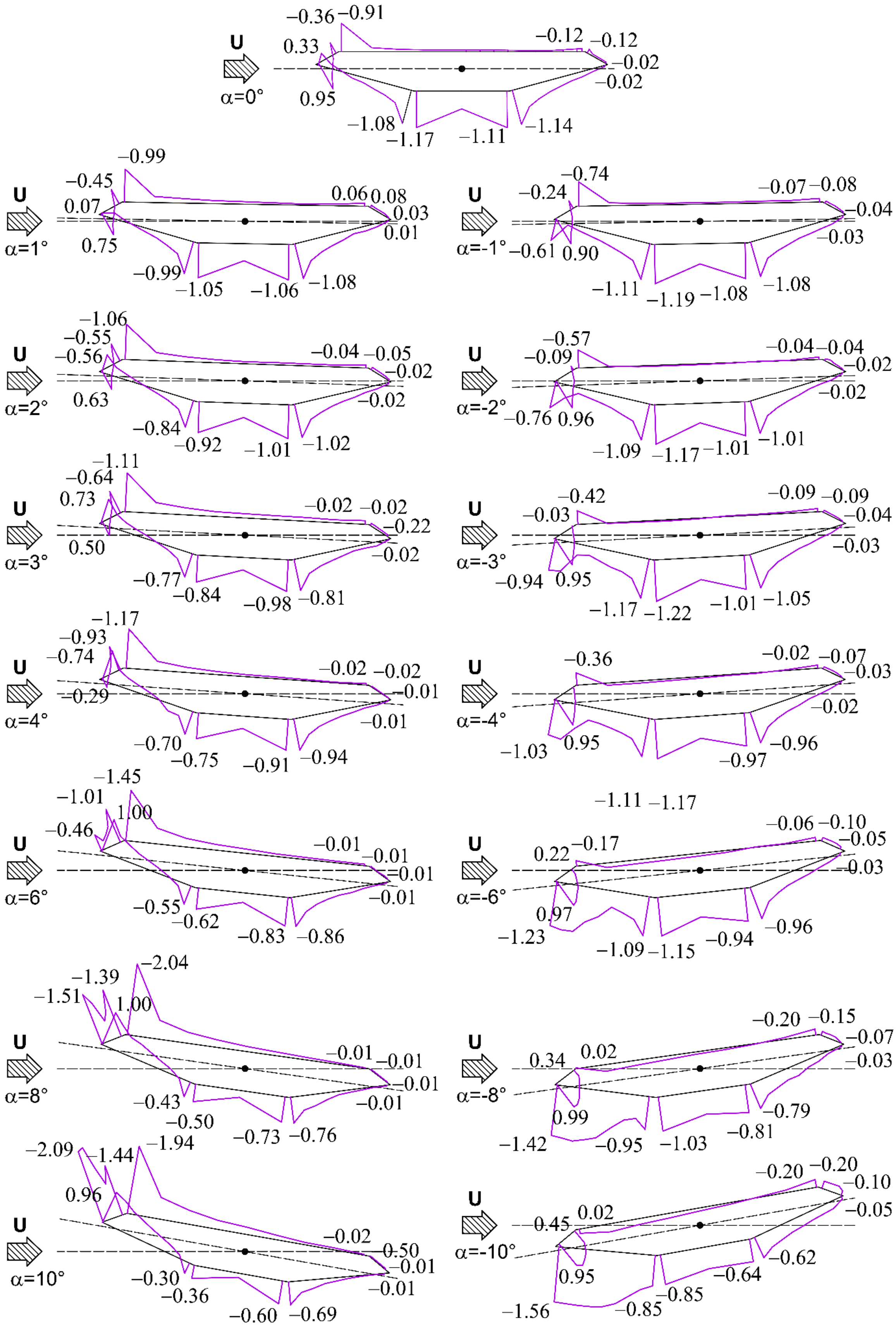

Figure 6

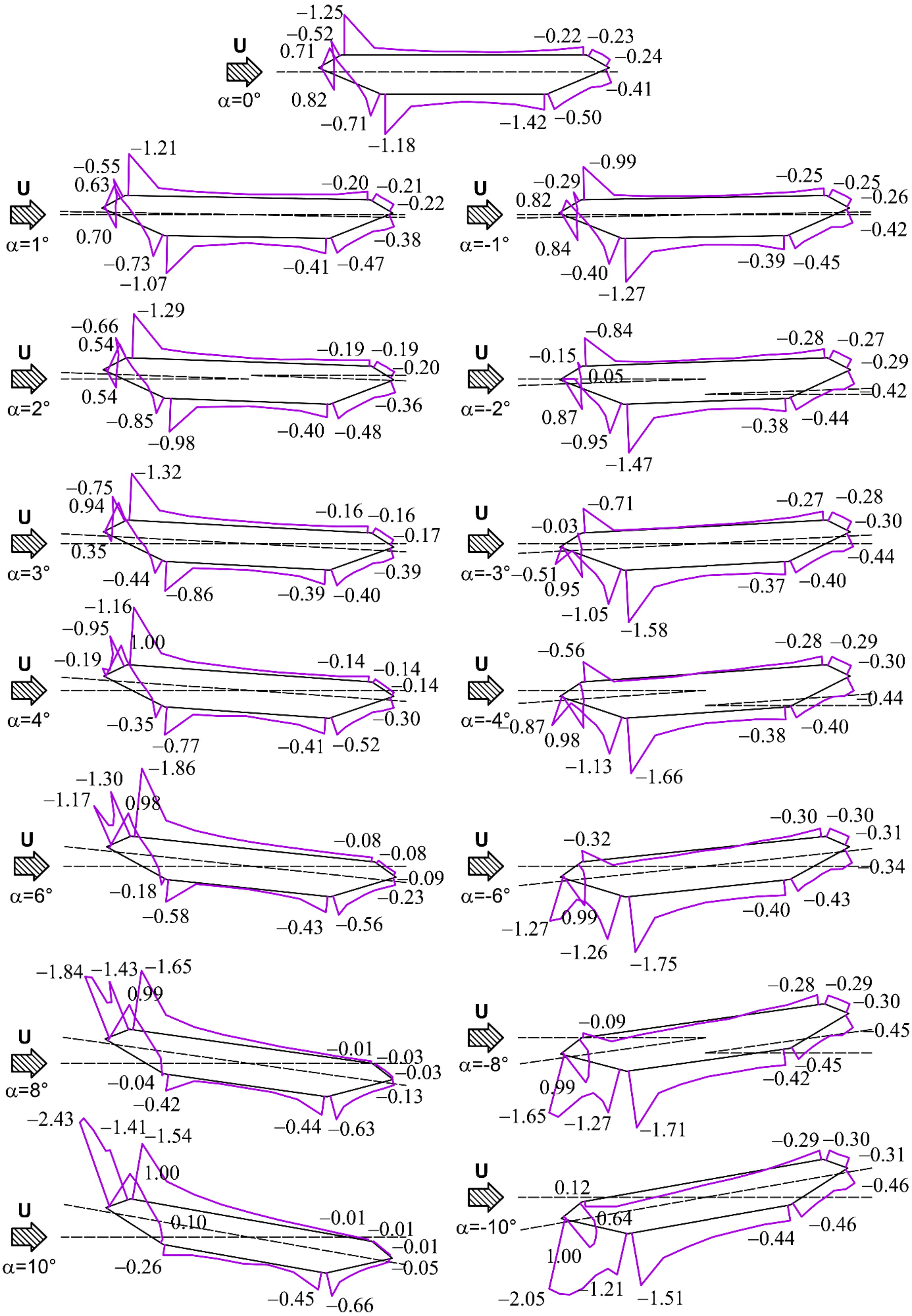
U
α=0°
−1.25
−0.52
0.71
0.82
−0.71
−1.18
−1.42
−0.50
−0.22
−0.23
−0.24
−0.41
α=1°
α=-1°
α=2°
α=-2°
α=3°
α=-3°
α=4°
α=-4°
α=6°
α=-6°
α=8°
α=-8°
α=10°
α=-10°

Figure 7

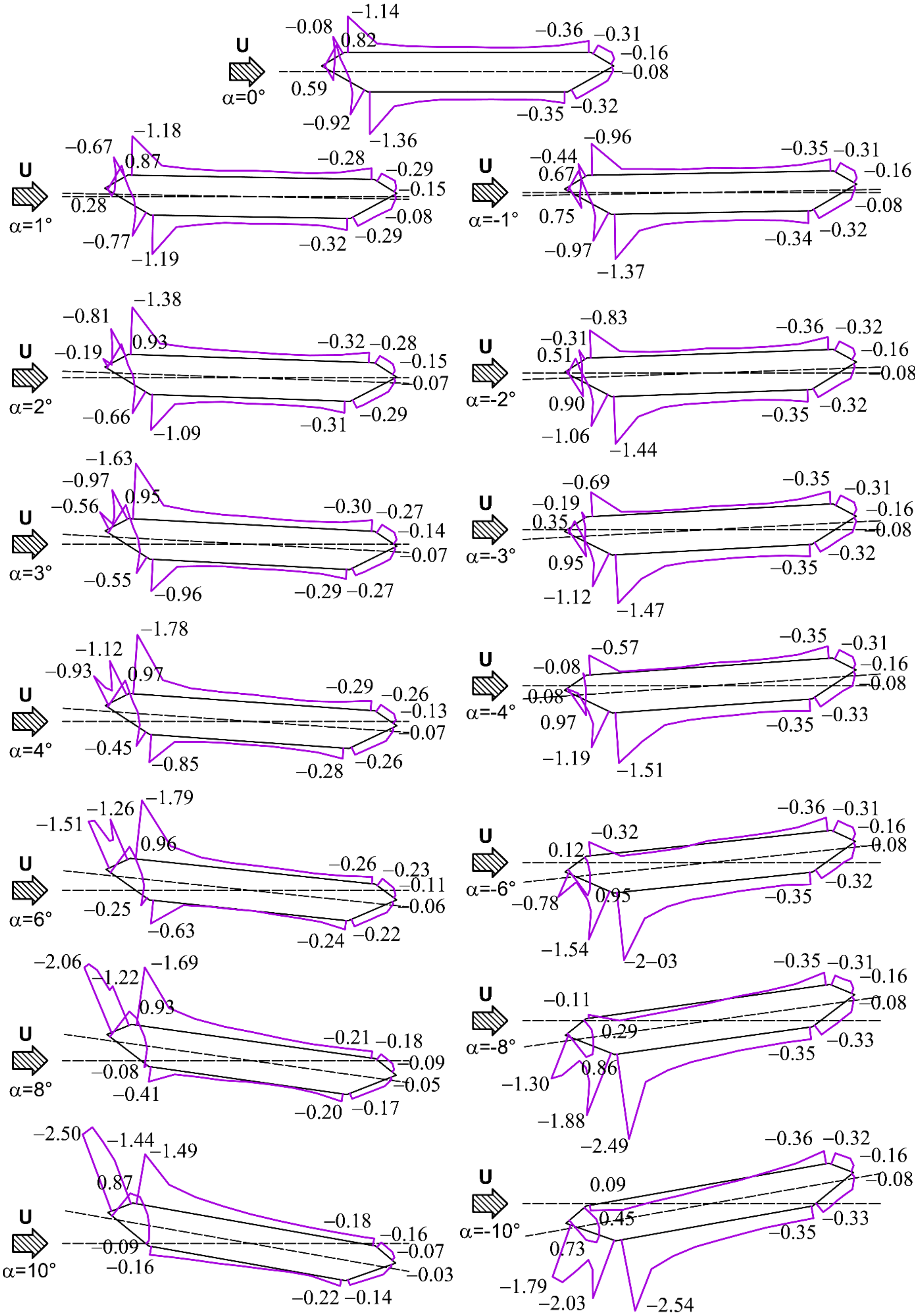

Figure 8

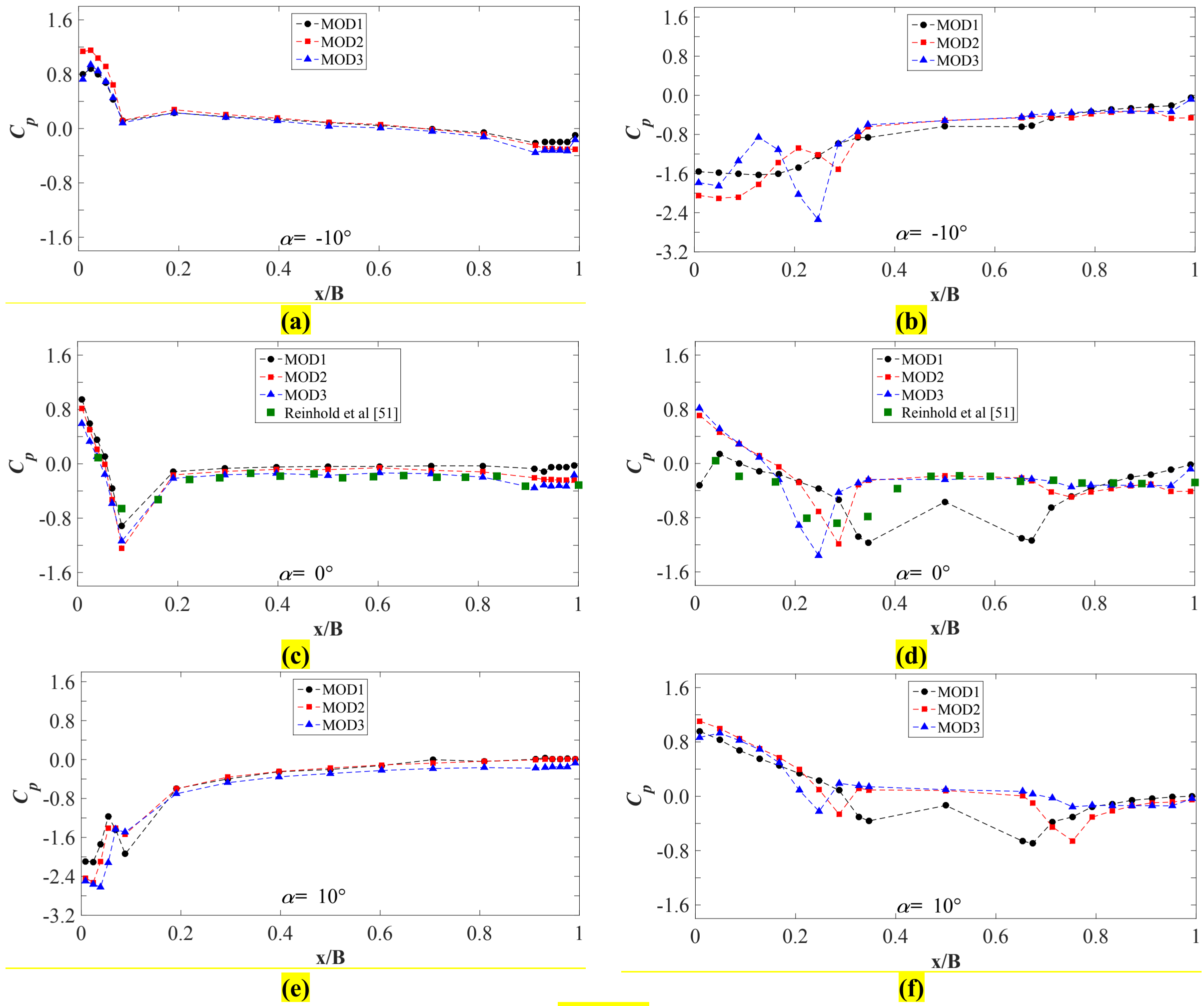

MOD1
MOD2
MOD3
Reinhold et al [51]
C_p
x/B
α= -10°
α= 0°
α= 10°
(a)
(b)
(c)
(d)
(e)
(f)

Figure 9

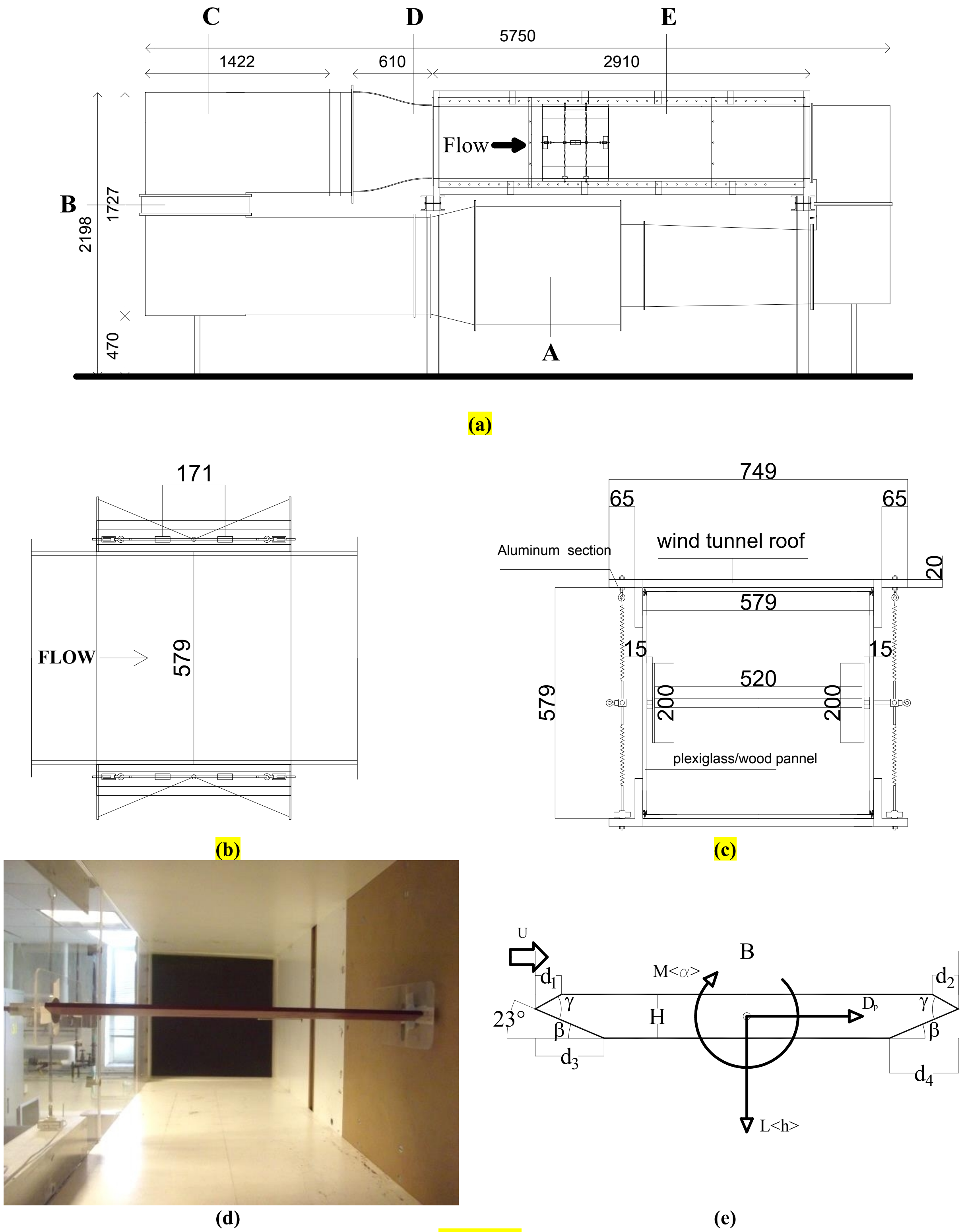
C
D
E
5750
1422
610
2910
Flow
B
1727
2198
470
A
(a)
171
FLOW
579
(b)
749
65
65
Aluminum section
wind tunnel roof
20
579
15
15
520
579
200
200
plexiglass/wood pannel
(c)
(d)
U
B
M<α>
d_1
d_2
γ
γ
23°
H
D_p
β
β
d_3
d_4
L<h>
(e)

Figure 10

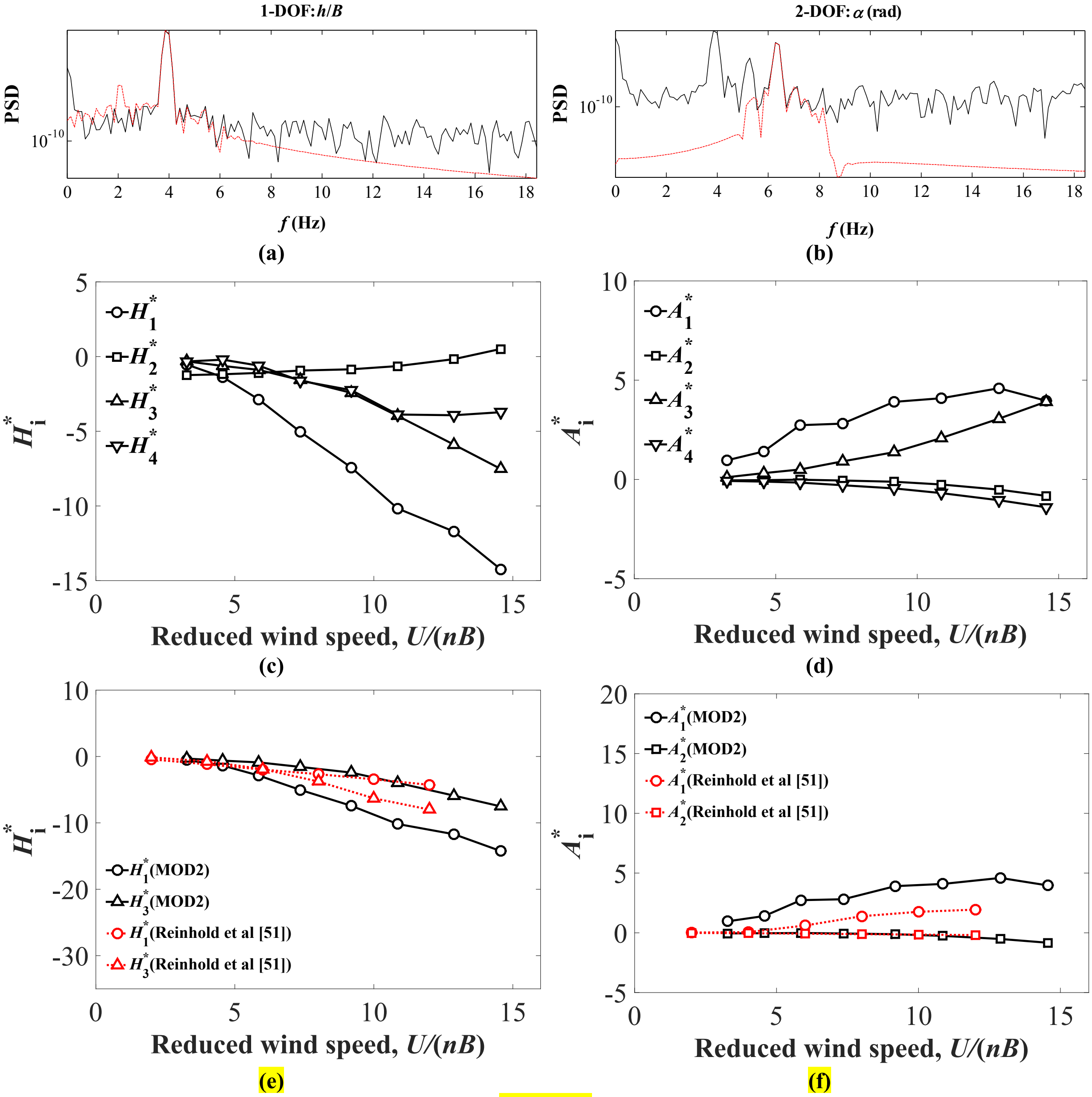

1-DOF: h/B
PSD
f (Hz)
(a)
2-DOF: α (rad)
PSD
f (Hz)
(b)
Reduced wind speed, U/(nB)
(c)
Reduced wind speed, U/(nB)
(d)
H1*(MOD2)
H3*(MOD2)
H1*(Reinhold et al [51])
H3*(Reinhold et al [51])
Reduced wind speed, U/(nB)
(e)
A1*(MOD2)
A2*(MOD2)
A1*(Reinhold et al [51])
A2*(Reinhold et al [51])
Reduced wind speed, U/(nB)
(f)

Figure 11

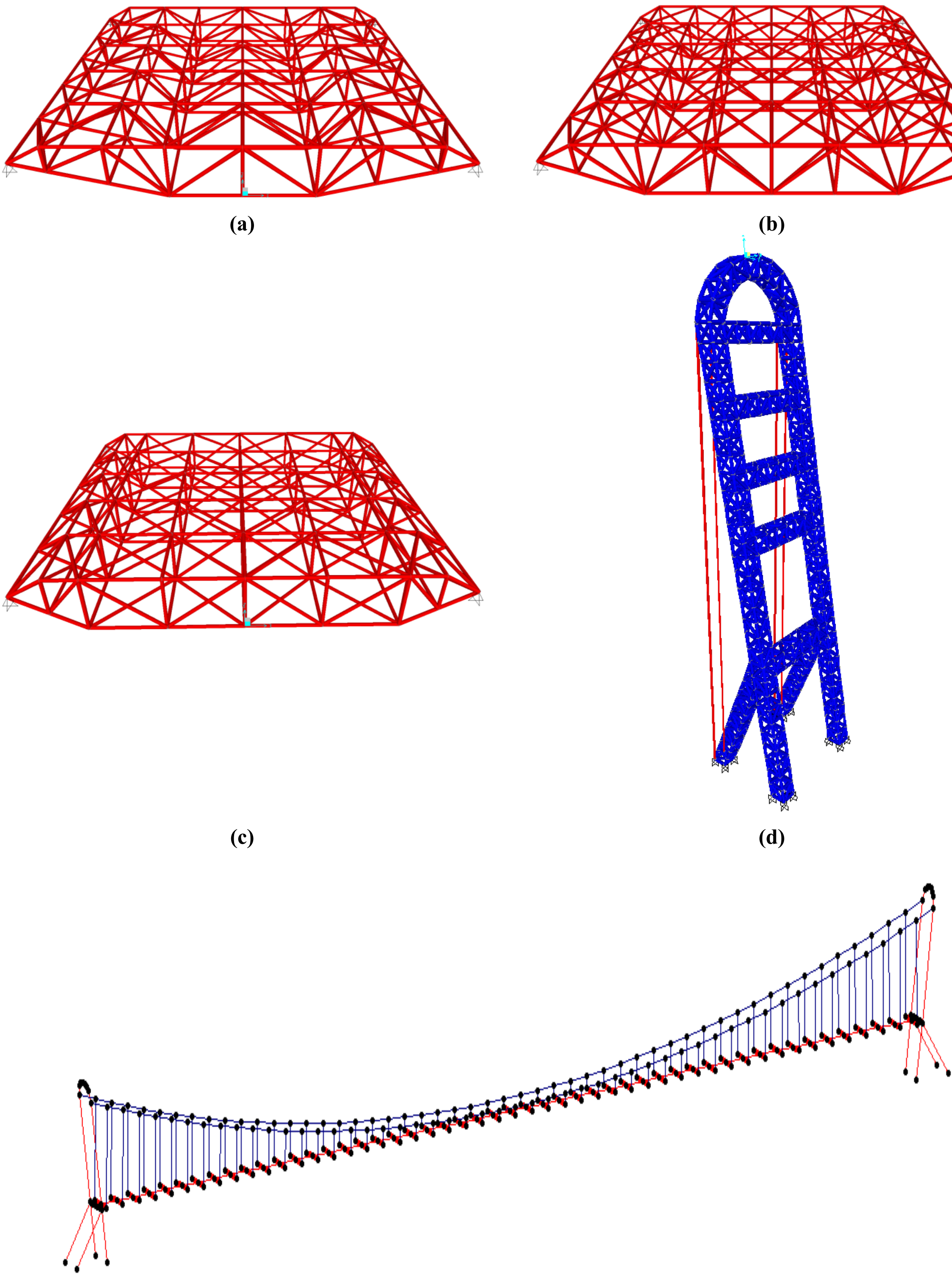

(a) (b) (c) (d) (e)

Figure 12

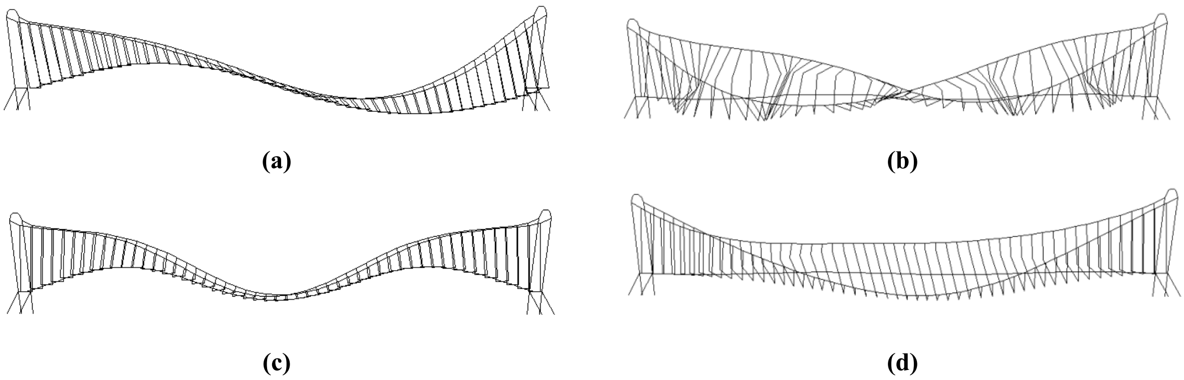

Figure 13

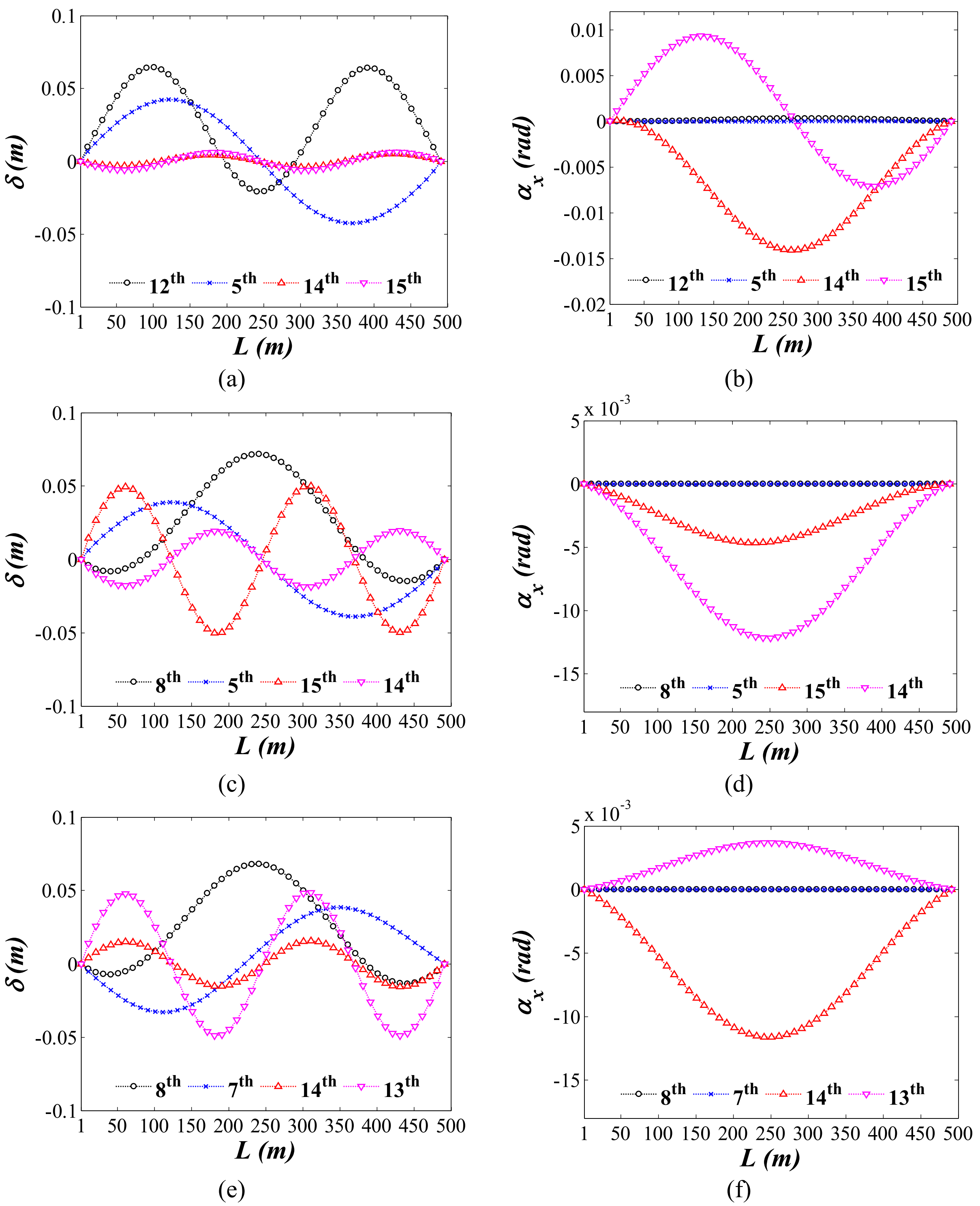

Figure 14

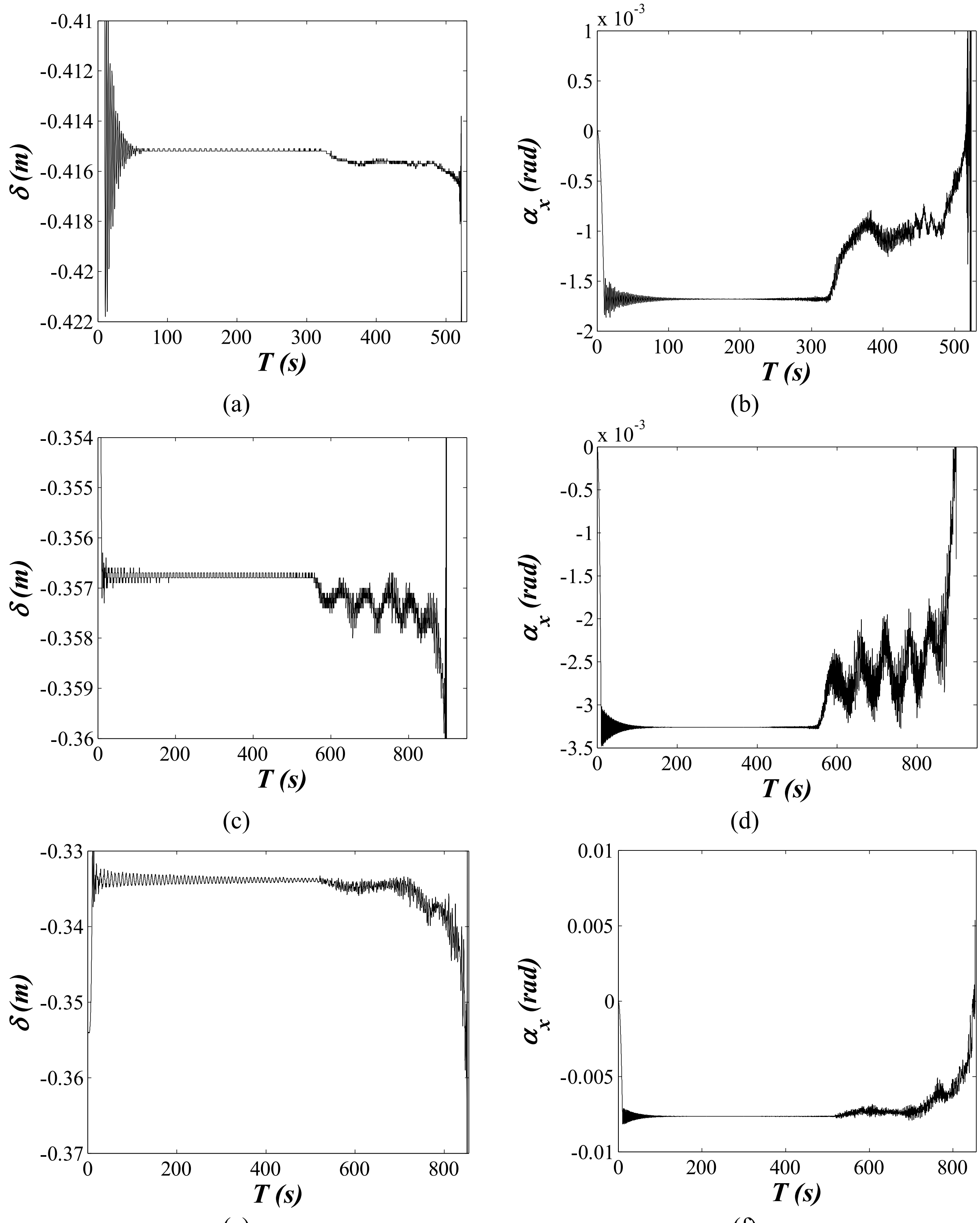

-0.41
-0.412
-0.414
-0.416
-0.418
-0.42
-0.422
δ (m)
0
100
200
300
400
500
T (s)
(a)
x 10^-3
1
0.5
0
-0.5
-1
-1.5
-2
α_x (rad)
T (s)
(b)
-0.354
-0.355
-0.356
-0.357
-0.358
-0.359
-0.36
δ (m)
600
800
T (s)
(c)
x 10^-3
-2.5
-3
-3.5
α_x (rad)
T (s)
(d)
-0.33
-0.34
-0.35
-0.36
-0.37
δ (m)
T (s)
(e)
0.01
0.005
0
-0.005
-0.01
α_x (rad)
T (s)
(f)

Figure 15

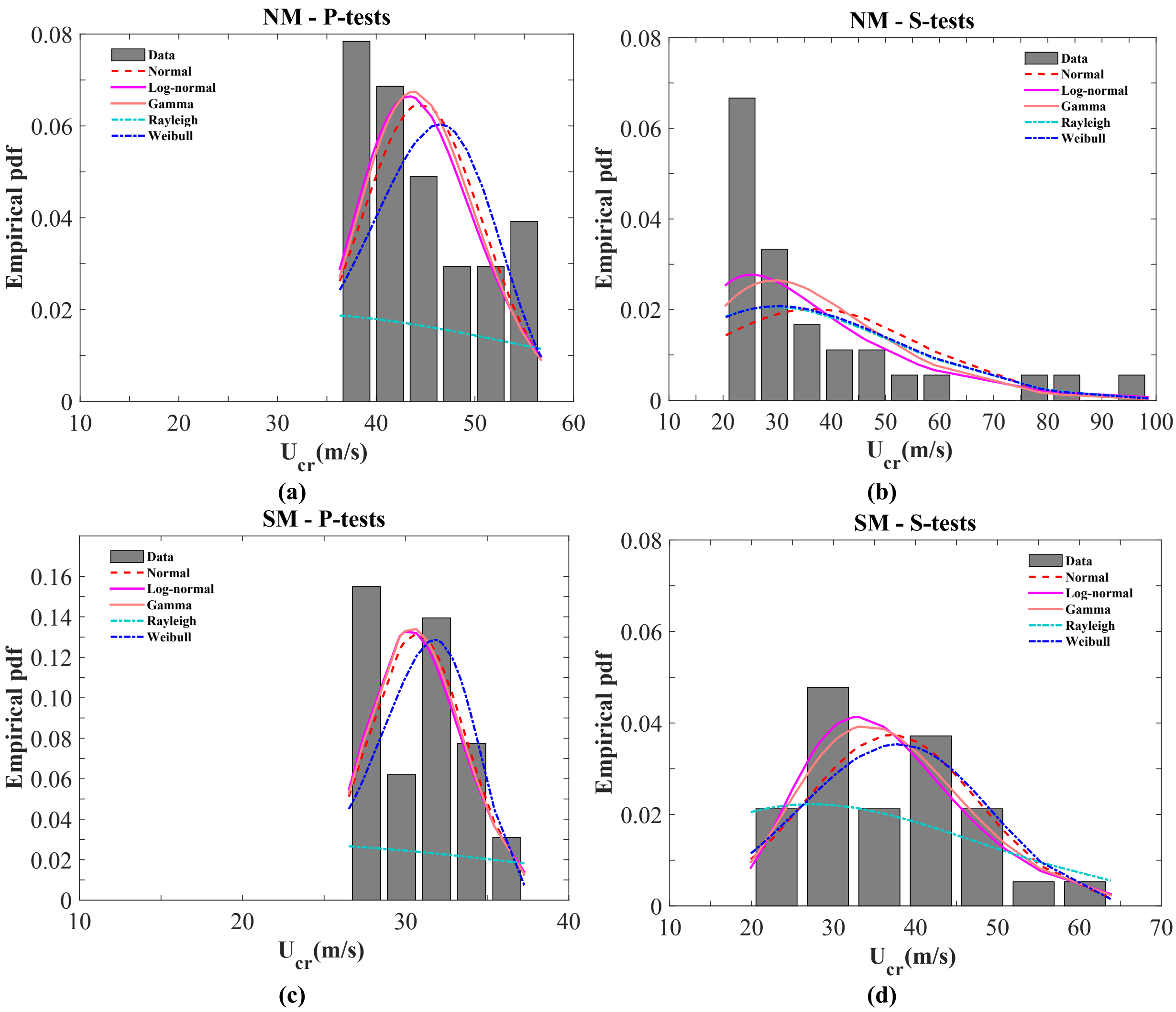
NM - P-tests
Data
Normal
Log-normal
Gamma
Rayleigh
Weibull
Empirical pdf
0
0.02
0.04
0.06
0.08
10
20
30
40
50
60
U_{cr}(m/s)
(a)
NM - S-tests
Data
Normal
Log-normal
Gamma
Rayleigh
Weibull
Empirical pdf
0
0.02
0.04
0.06
0.08
10
20
30
40
50
60
70
80
90
100
U_{cr}(m/s)
(b)
SM - P-tests
Data
Normal
Log-normal
Gamma
Rayleigh
Weibull
Empirical pdf
0
0.02
0.04
0.06
0.08
0.10
0.12
0.14
0.16
10
20
30
40
U_{cr}(m/s)
(c)
SM - S-tests
Data
Normal
Log-normal
Gamma
Rayleigh
Weibull
Empirical pdf
0
0.02
0.04
0.06
0.08
10
20
30
40
50
60
70
U_{cr}(m/s)
(d)

Figure 16

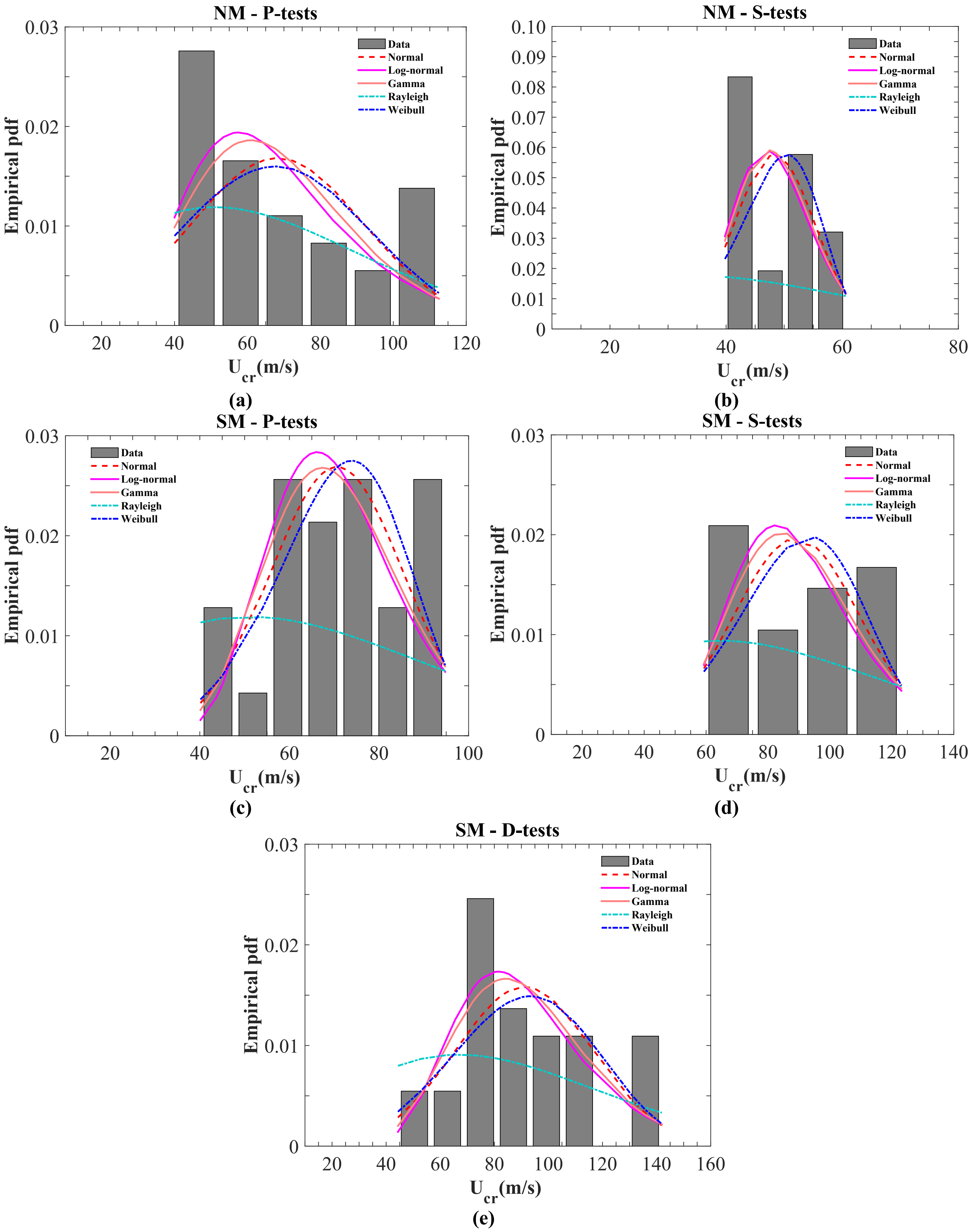
NM - P-tests
Empirical pdf
U_{cr}(m/s)
Data
Normal
Log-normal
Gamma
Rayleigh
Weibull
(a)
NM - S-tests
(b)
SM - P-tests
(c)
SM - S-tests
(d)
SM - D-tests
(e)

Figure 17

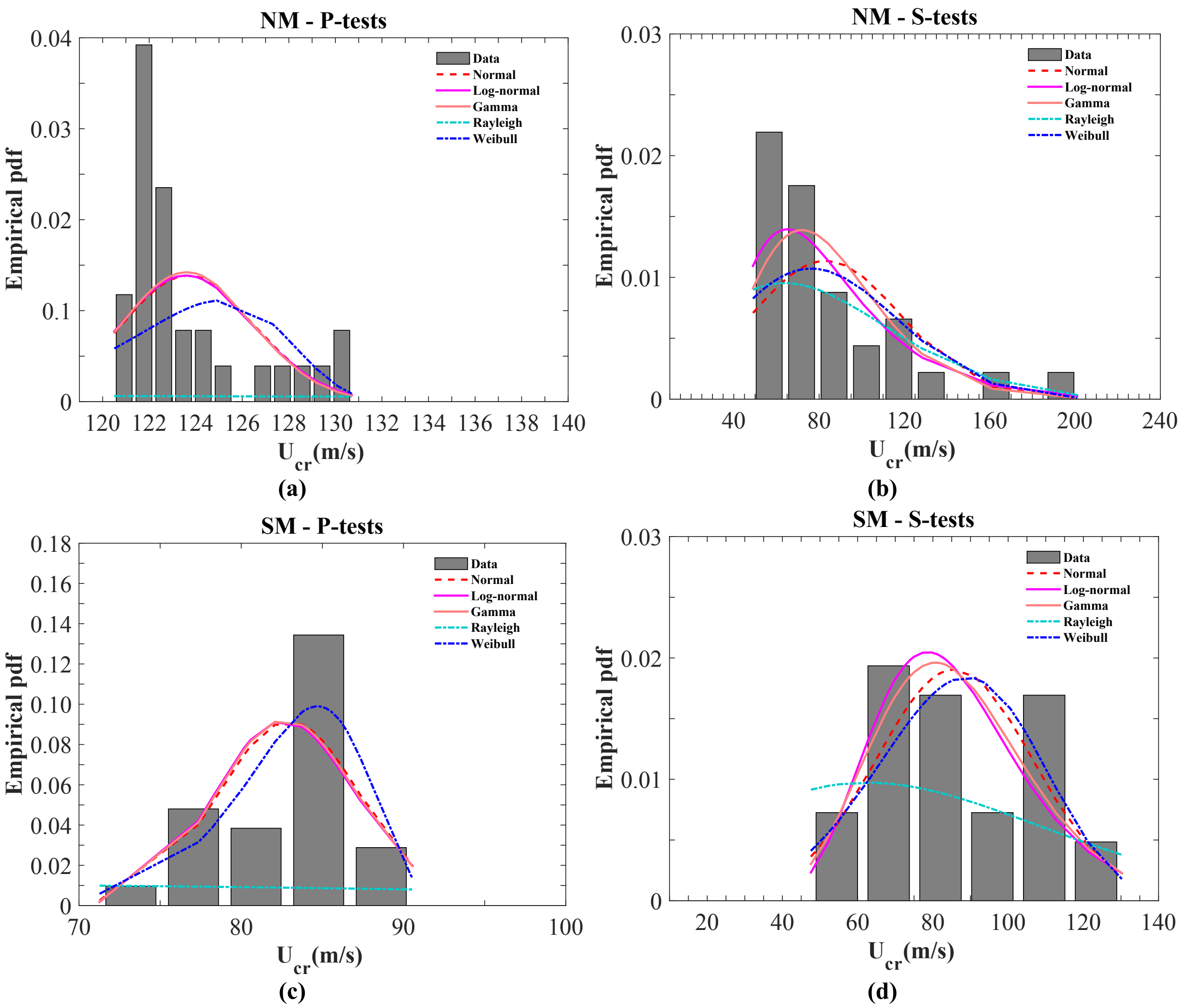
NM - P-tests
Empirical pdf
Data
Normal
Log-normal
Gamma
Rayleigh
Weibull
U cr(m/s)
(a)
NM - S-tests
(b)
SM - P-tests
(c)
SM - S-tests
(d)

Figure 18

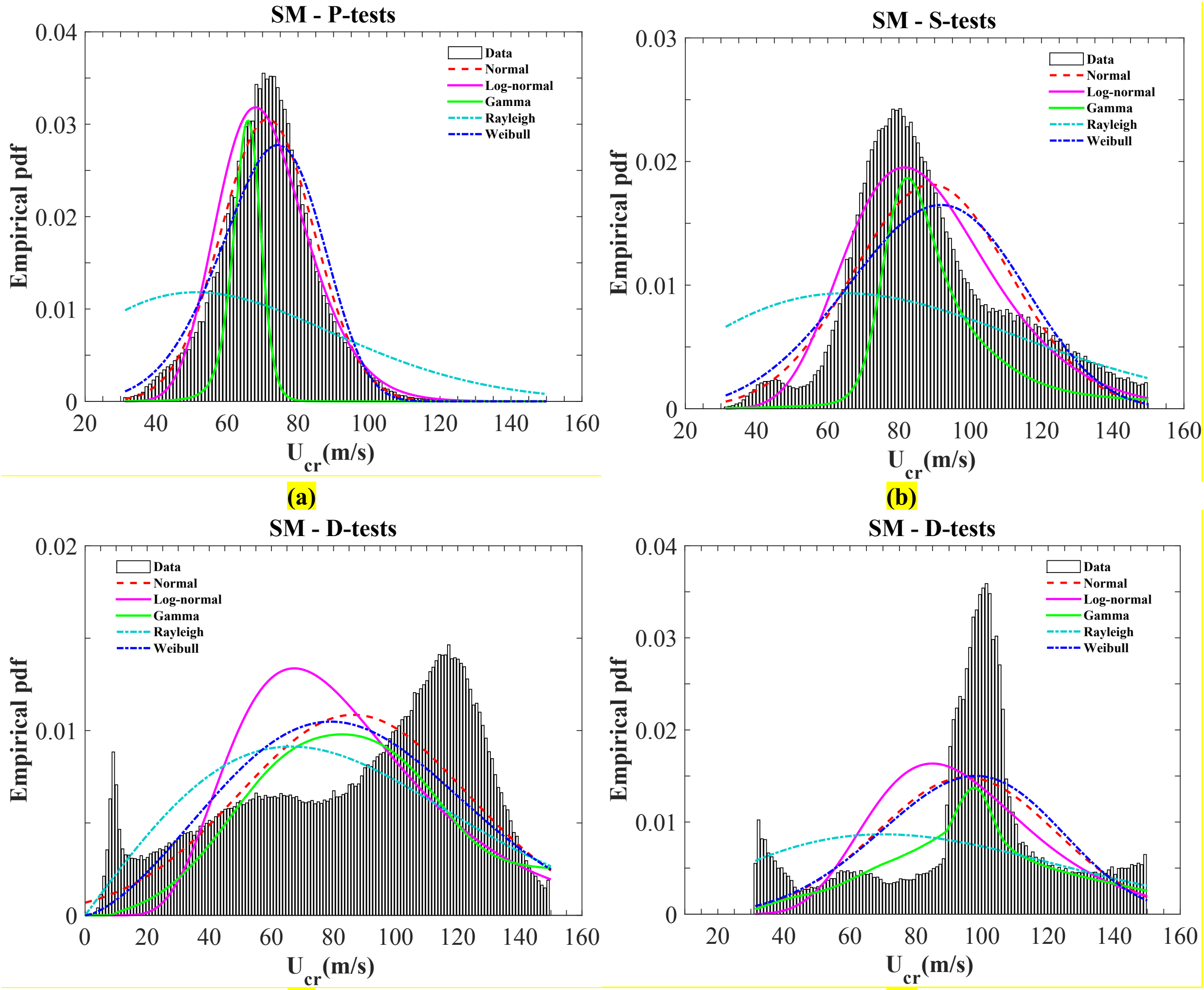

(a) (b) (c) (d)

Figure 19

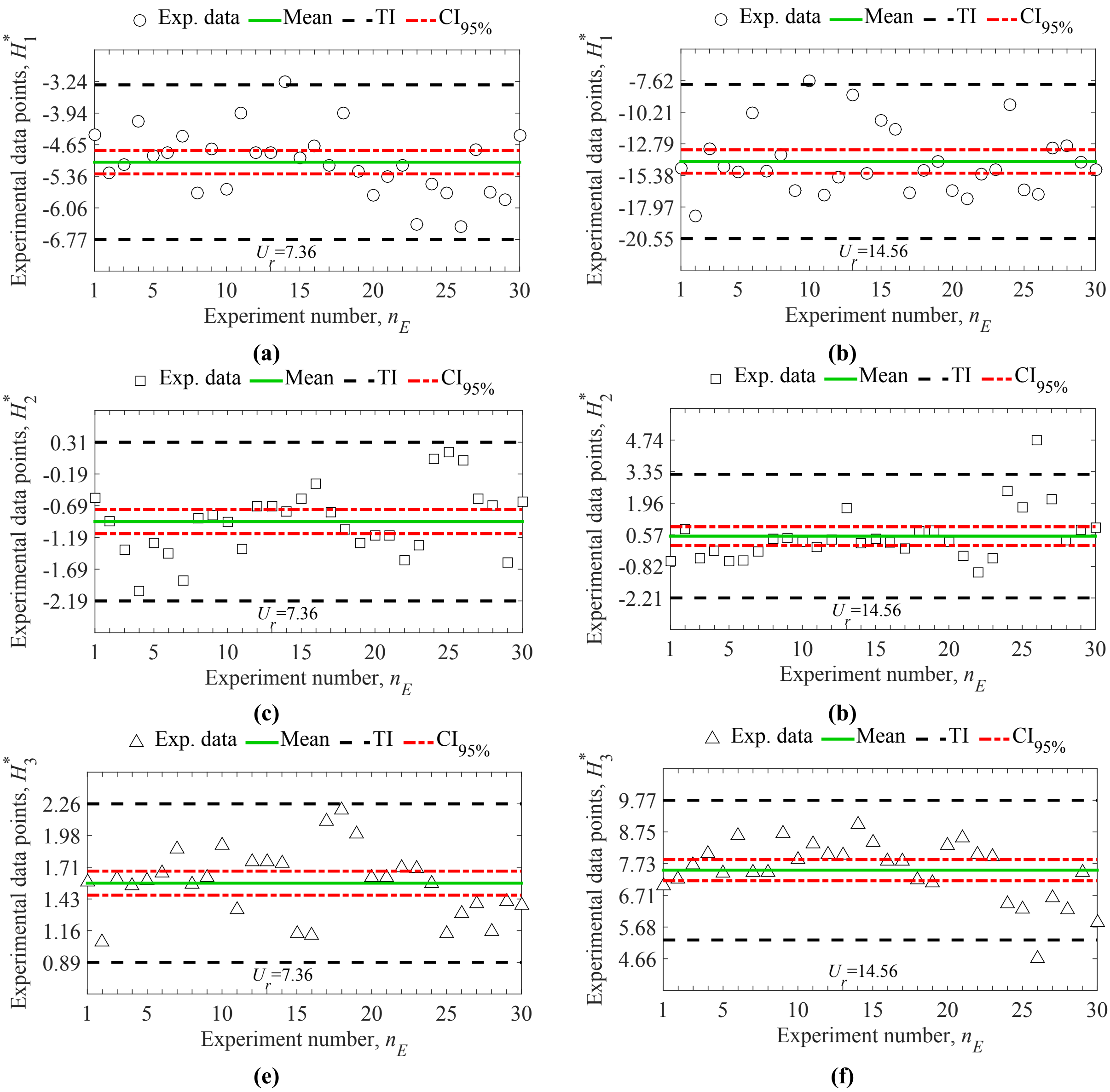

Exp. data
Mean
TI
CI95%
Experimental data points, H*1
-3.24
-3.94
-4.65
-5.36
-6.06
-6.77
Ur=7.36
Experiment number, nE
(a)
-7.62
-10.21
-12.79
-15.38
-17.97
-20.55
Ur=14.56
(b)
Experimental data points, H*2
0.31
-0.19
-0.69
-1.19
-1.69
-2.19
(c)
4.74
3.35
1.96
0.57
-0.82
-2.21
(b)
Experimental data points, H*3
2.26
1.98
1.71
1.43
1.16
0.89
(e)
9.77
8.75
7.73
6.71
5.68
4.66
(f)

Figure 20

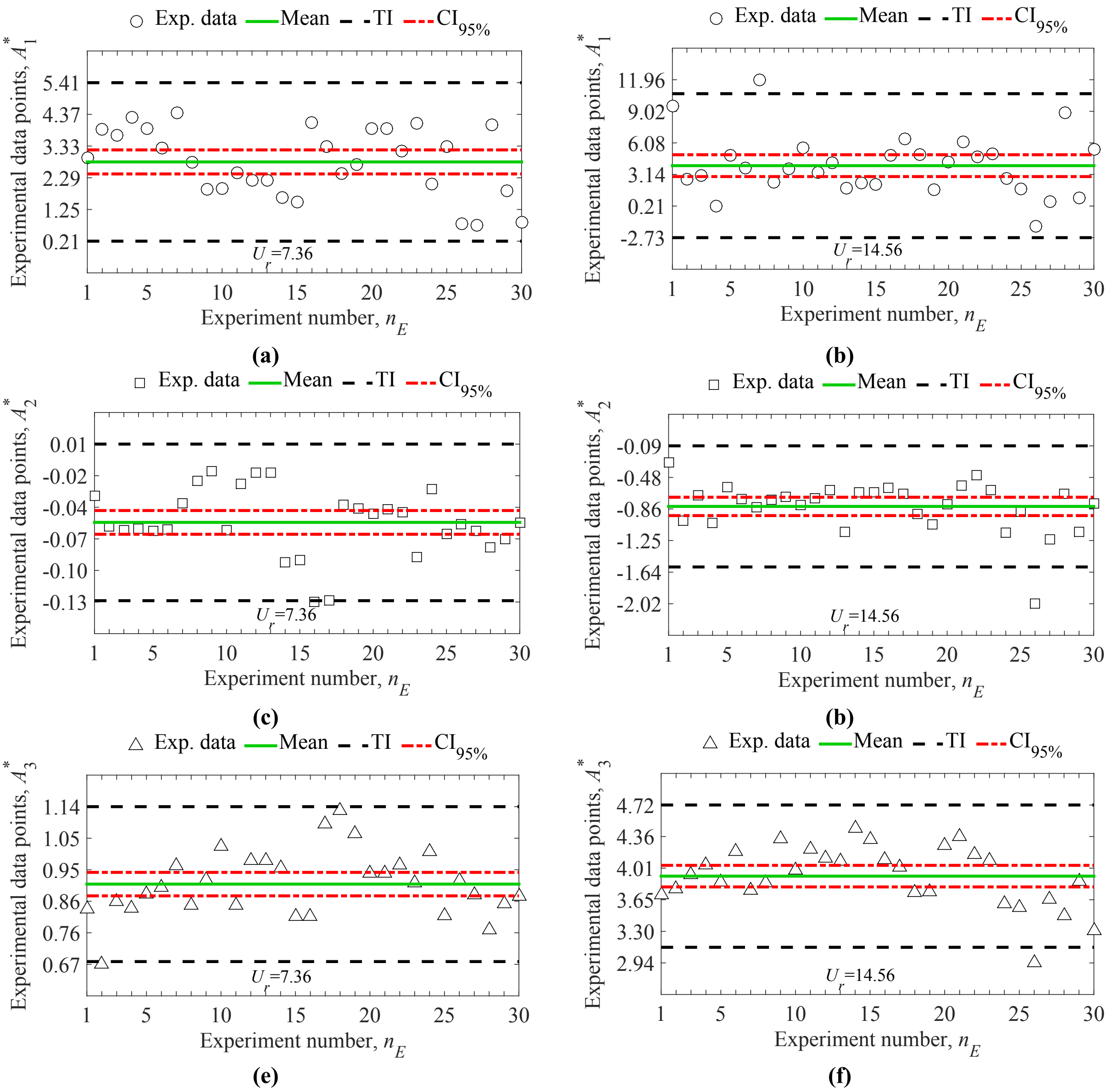
Exp. data
Mean
TI
CI95%
Experimental data points, A*1
Experimental data points, A*2
Experimental data points, A*3
Experiment number, nE
Ur=7.36
Ur=14.56
5.41
4.37
3.33
2.29
1.25
0.21
11.96
9.02
6.08
3.14
0.21
-2.73
0.01
-0.02
-0.04
-0.07
-0.10
-0.13
-0.09
-0.48
-0.86
-1.25
-1.64
-2.02
1.14
1.05
0.95
0.86
0.76
0.67
4.72
4.36
4.01
3.65
3.30
2.94
1
5
10
15
20
25
30
(a)
(b)
(c)
(b)
(e)
(f)

Figure 21